Marine and Petroleum Geology 58 (2014) 139–167

Contents lists available at ScienceDirect

Marine and Petroleum Geology

journal homepage: www.elsevier.com/locate/marpetgeo

Research paper

Comparison of the physical and geotechnical properties of gas-hydrate-bearing sediments from offshore India and other gas-hydrate-reservoir systems

W.J. Winters [a, *], R.W. Wilcox-Cline [a], P. Long [b], S.K. Dewri [c], P. Kumar [c], L. Stern [d], L. Kerr [e]

[a] U.S. Geological Survey, 384 Woods Hole Road, Woods Hole, MA 02543, USA
[b] Lawrence Berkeley National Laboratory, Earth Sciences Division, 1 Cyclotron Road, MS74RR316C, Berkeley, CA 94720, USA
[c] Oil and Natural Gas Corporation Ltd., ONGC Complex, Phase 2, Panvel, Navi-Mumbai 410 221, India
[d] U.S. Geological Survey, 345 Middlefield Road, Menlo Park, CA 94025, USA
[e] Marine Biological Laboratory, 7 MBL Street, Woods Hole, MA 02543, USA

ARTICLE INFO

Article history:
Received 6 December 2013
Received in revised form
18 July 2014
Accepted 23 July 2014
Available online 9 September 2014

Keywords:
Physical properties
Gas hydrate
Porosity
Atterberg limits
Consolidation
Permeability
Shear strength
Scanning electron microscopy

ABSTRACT

The sediment characteristics of hydrate-bearing reservoirs profoundly affect the formation, distribution, and morphology of gas hydrate. The presence and type of gas, porewater chemistry, fluid migration, and subbottom temperature may govern the hydrate formation process, but it is the host sediment that commonly dictates final hydrate habit, and whether hydrate may be economically developed.

In this paper, the physical properties of hydrate-bearing regions offshore eastern India (Krishna-Godavari and Mahanadi Basins) and the Andaman Islands, determined from Expedition NGHP-01 cores, are compared to each other, well logs, and published results of other hydrate reservoirs. Properties from the hydrate-free Kerala-Konkan basin off the west coast of India are also presented. Coarser-grained reservoirs (permafrost-related and marine) may contain high gas-hydrate-pore saturations, while finer-grained reservoirs may contain low-saturation disseminated or more complex gas-hydrates, including nodules, layers, and high-angle planar and rotational veins. However, even in these fine-grained sediments, gas hydrate preferentially forms in coarser sediment or fractures, when present. The presence of hydrate in conjunction with other geologic processes may be responsible for sediment porosity being nearly uniform for almost 500 m off the Andaman Islands.

Properties of individual NGHP-01 wells and regional trends are discussed in detail. However, comparison of marine and permafrost-related Arctic reservoirs provides insight into the inter-relationships and common traits between physical properties and the morphology of gas-hydrate reservoirs regardless of location. Extrapolation of properties from one location to another also enhances our understanding of gas-hydrate reservoir systems. Grain size and porosity effects on permeability are critical, both locally to trap gas and regionally to provide fluid flow to hydrate reservoirs. Index properties corroborate more advanced consolidation and triaxial strength test results and can be used for predicting behavior in other NGHP-01 regions. Pseudo-overconsolidation is present near the seafloor and is underlain by underconsolidation at depth at some NGHP-01 locations.

Published by Elsevier Ltd.

1. Introduction

The characteristics of host sediment have a profound effect on the morphology, pore saturation, and habit of naturally-occurring gas hydrate (GH). In addition, significant hydrate formation or dissociation can alter the mechanical, acoustic, and hydraulic properties and behavior of marine and permafrost-related Arctic sedimentary reservoirs enhancing or adversely affecting exploration and production programs. Grain size and other related sediment properties (for example, porosity and permeability) often determine the production potential of a hydrate-bearing reservoir. Accurate knowledge of sediment physical properties is also necessary for borehole stability calculations and design of production-related components such as filters to prevent clogging by sediment migration (Lee et al., 2013). In addition, correlations

* Corresponding author. Tel.: +1 508 548 7365.
E-mail address: hydrates92@comcast.net (W.J. Winters).

http://dx.doi.org/10.1016/j.marpetgeo.2014.07.024
0264-8172/Published by Elsevier Ltd.

Nomenclature

A	Change in pore pressure/change in deviator stress [kPa/kPa]
ASTM	American Society for Testing and Materials
AT	Atwater Valley
BSR	Bottom Simulating Reflector
c'	Effective cohesion intercept [kPa]
C_c	Compression index
$C_{c\varepsilon}$	Modified compression index
CH	Clay, high plasticity
C_r	Recompression index
c_v(in situ)	Coeff. of consolidation (in situ stress) [m^2/s]
c_v(max)	Coeff. of consolidation (maximum past stress) [m^2/s]
c_v(virgin)	Coeff. of consolidation (virgin compression ave.) [m^2/s]
D_{90}	Diameter at which 90% of the sample is finer
D_{50}	Median grain size
D_{10}	Diameter at which 10% of the sample is finer
e_o	Void ratio (initial), initial volume of voids/volume solids
e_f	Void ratio (final), final volume of voids/volume solids
ER	Electrical resistivity
GH	Gas hydrate
GHB	Gas hydrate bearing
GoM	Gulf of Mexico
JIP	Joint Industry Project
ka	Thousand years before present
KC	Keathley Canyon
KSDR	Schlumberger-Doll Research permeability log
KG	Krishna-Godavari Basin
KK	Kerala-Konkan Basin
LI	Liquidity Index = (wc−PL)/(LL−PL)
LL	Liquid limit
MAD	Moisture and density sample
MB	Microbiology
mbsf	meters below seafloor
mD	millidarcy
MD	Marion Dufresne
MGS	Mean grain size
MH	Silt, high compressibility
n	porosity
NGHP-01	National Gas Hydrate Program (of India) Exp. 01
NWT	Northwest Territories, Canada
OCR	Overconsolidation ratio
OH	Organics, high compressibility
p'	Normal effective stress acting on a plane inclined at 45° from the horizontal, $(\sigma'_1 + \sigma'_3)/2$ [kPa]
PI	Plasticity Index = LL−PL
PL	Plastic limit
PP	Physical properties
PW	Pore water
q	Shear stress acting on a plane inclined at 45° from the horizontal, $(\sigma_1-\sigma_3)/2$ [kPa]
RKB	Relative to the Kelly bushing on a drill rig
S_h	Hydrate pore saturation
S_{pp}	Undrained shear strength (1/2 the instrument-reading unconfined compressive strength) determined with a Pocket Penetrometer [kPa]
S_t	Sensitivity (undrained peak strength/remolded strength)
S_u/p'	Undrained shear strength/consolidation stress [kPa/kPa]
S_v	Vane shear strength [kPa]
TCM	Trillion cubic meters
US DOE	U.S. Department of Energy
USGS	U.S. Geological Survey
wc	Water content, mass water/mass solids [%]
σ'_{vo}	In situ vertical effective stress [kPa]
σ'_{vm}	Maximum past stress [kPa]
σ'_e	Excess effective stress [kPa]
φ'	Friction angle in terms of effective stresses [degrees]
φ'_{max}	Maximum friction angle in terms of effective stresses, passing through the origin [degrees]

between various properties lead to a better understanding of diagenesis and geologic history (Taylor, 1991).

All other factors being equal, sediment properties greatly influence hydrate formation. This occurs both locally as a reservoir for individual hydrate grains and assemblages and also on a much larger scale by influencing fault patterns and characteristics (Minor and Hudson, 2006) that are responsible for regional fluid and gas flow that feed hydrate reservoirs (e.g., Riedel et al., 2010a). Furthermore, faults might serve as mechanisms to locally change sediment porosity (Busch, 1989).

Since 1995, the U.S. Geological Survey (USGS), in cooperation with the U.S. Department of Energy, Gulf of Mexico Joint Industry Project, National Gas Hydrate Program of India, Canadian Geological Survey, Ocean Drilling Program, Integrated Ocean Drilling Program, BP Exploration-Alaska, Japan Oil Gas and Metals National Corporation, Japan Petroleum Exploration Co., International Marine Past Global Changes Study (IMAGES) program, and Paleoceanography of the Atlantic and Geochemistry (PAGE) program, has been determining physical properties of marine and permafrost-related Arctic sediments and their relation to the presence of GH.

Mounting evidence suggests that the formation and preservation of significant natural gas hydrate requires the elements of a petroleum system (Collett et al., 2009, 2011). Those features typically include: (a) appropriate reservoir physical properties, (b) a source of adequate gas supply, (c) sufficient water without high brine content or other detrimental geochemical contaminants, (d) migration pathway(s) for water and gas, (e) a trap and seal, and (f) proper timing relative to temperature and other environmental influences (Collett, 2008; Hunter et al., 2008).

After more than a decade of study, enough physical properties data exist on sediments that host gas hydrates from a wide variety of settings around the globe to make preliminary assessments on how these sediment properties affect the type and distribution of gas hydrates (Boswell and Collett, 2011). Dai et al. (2012) presents criteria that relate grain-particle diameter D_{10} and effective stress with gas-hydrate morphology. Pore-filling hydrate is present in coarse-grained sands at high effective stress, fine-grained sand, and coarse silt; nodules that displace sediment in all directions form in fine-grained sediment at low effective stress; and hydrate lenses or veins displace sediment in the direction of the smallest effective stress as they form in intermediate conditions. Disseminated GH of low pore saturation is also widespread in fine-grained sediment.

This paper presents and compares the results of nine physical property test programs conducted on marine and permafrost-related sediment (Table 1, Fig. 1) and enhances the work of Winters (2011) by presenting infrared and SEM images, statistics, and property profiles. Major emphasis is placed on the 2006 National Gas Hydrate Program of India Expedition 01 (NGHP-01)

Table 1
Project and site information, including general project, and specific USGS physical-property references.

Project	Area	Region	Boring ID	Latitude (deg.)	Longitude (deg.)	Water depth (marine projects) (m)	Primary reference	Primary USGS physical property reference
Marine								
NGHP-01	W coast India	KK Basin	01A	15.3061 N	70.9032 E	~2663	Collett et al., 2008a,b	This paper; Winters, 2011
	E coast India	KG Basin	10D	15.8644 N	81.8345 E	~1038		
	E coast India	KG Basin	15A	16.0950N	82.1624E	~926		
	Andaman Sea	Andaman Is	17A	10.7532 N	93.1123 E	~1344		
	NE coast India	Mahanadi Basin	18A	19.1524 N	85.7729 E	~1374		
	NE coast India	Mahanadi Basin	19A	18.9776 N	85.6587 E	~1422		
IODP X311	Vancouver Is	Midslope	U1327C	48.6981 N	126.8652 W	1304	Riedel et al., 2006	This paper; Winters, 2011
		Eastern	U1329C	48.7896 N	126.6787 W	946		
ODP Leg 204	Oregon coast	Hydrate Ridge	1249	44.5702 N	125.1474 W	778	Shipbpard scientific party, 2003	Winters et al., 2006
MD02	S coast USA	N GoM	Various	–	–	–	Winters et al., 2007a	Winters et al., 2007c
JIP Leg 1	S USA (GoM)	Atwater Valley	AT13-2	27.9471 N	89.2893 W	1291	Ruppel et al., 2008	Winters et al., 2008a
		AT mound	ATM1	27.9366 N	89.2795 W	1296		
		AT mound	ATM2	27.9366 N	89.2797 W	1295		
		Keathley Canyon	KC151-3	26.8230 N	92.9867 W	1322		
ODP Leg 164	SE coast USA	Blake Ridge	995A	31.8035 N	75.5224 W	2778	Paull et al., 1996	Winters, 2000b
Arctic						El. ASL (m)		
Mount Elbert	N Alaska	North Slope	Mt Elbert	70.4556 N	149.4108 W	6.5	Hunter et al., 2011	Winters et al., 2011
Mallik	NWT, Canada	Mackenzie Delta	Mallik 5L-38	69.4609 N	134.6608 W	–	Dallimore and Collett, 2005	Winters et al., 2005
Mallik	NWT, Canada	Mackenzie Delta	Mallik 2L-38	69.4613 N	134.6584 W	–	Dallimore et al., 1999b	Winters et al., 1999a

ASL: Above sea level; AT: Atwater Valley; GoM: Gulf of Mexico; KK: Kerala-Konkan; KG: Krishna-Godavari.

(Fig. 2) (Collett et al., 2008a, 2008b) and to a lesser extent the 2005 Integrated Ocean Drilling Program (IODP) Expedition 311 (X311) (northern Cascadia margin) (Riedel et al., 2010b).

Nearly all samples described in this paper did not contain gas hydrate at the time of testing. Furthermore, hydrate dissociation between the time of core recovery and the measurement of physical properties is known to affect the remaining sediments (e.g., Waite et al., 2008). Even when hydrate was not present in the samples, the properties of surrounding sediment are still important since they often shed light on the conditions that controlled the formation of the gas hydrate. In addition, fundamental properties of sedimentary deposits and stress history are important for understanding regional and site-specific geology.

2. Geologic setting of study areas

Since 1995, field programs dedicated to the study of gas hydrates have been conducted world-wide in both marine and permafrost-related Arctic environments. Many of these programs have included a component to determine physical properties of reservoir material.

2.1. Marine

2.1.1. India (NGHP-01)

In 2006, a drilling expedition was conducted offshore India and along the Andaman convergent margin (Fig. 2) on the drillship

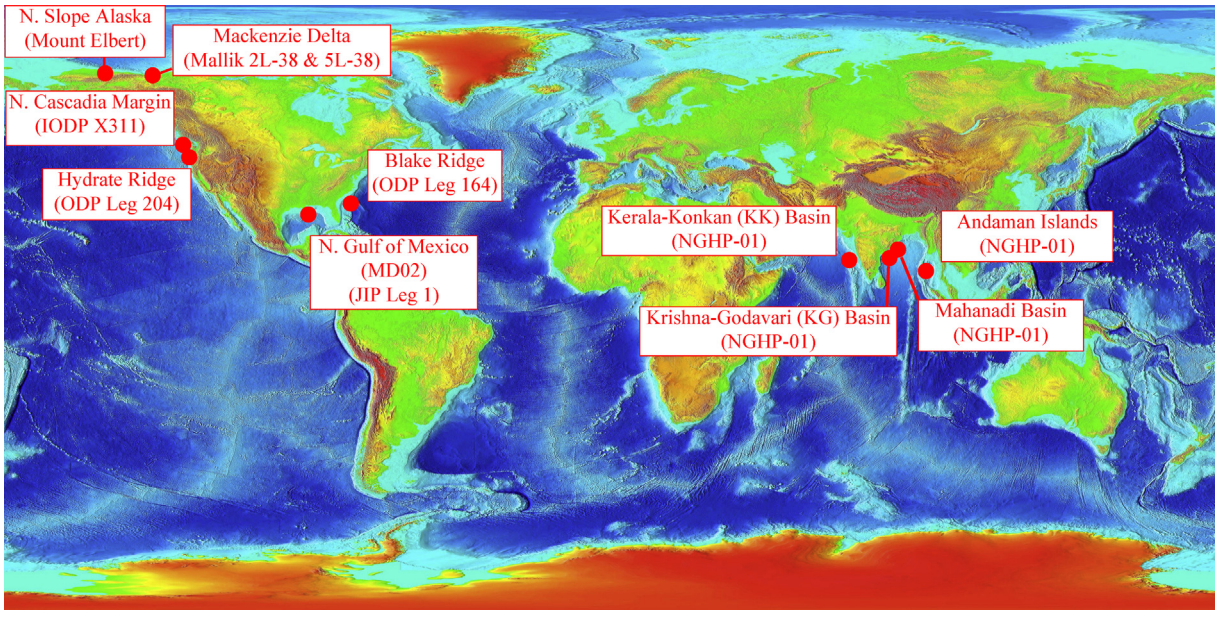

Figure 1. Projects that have had physical property measurements performed as part of this study.

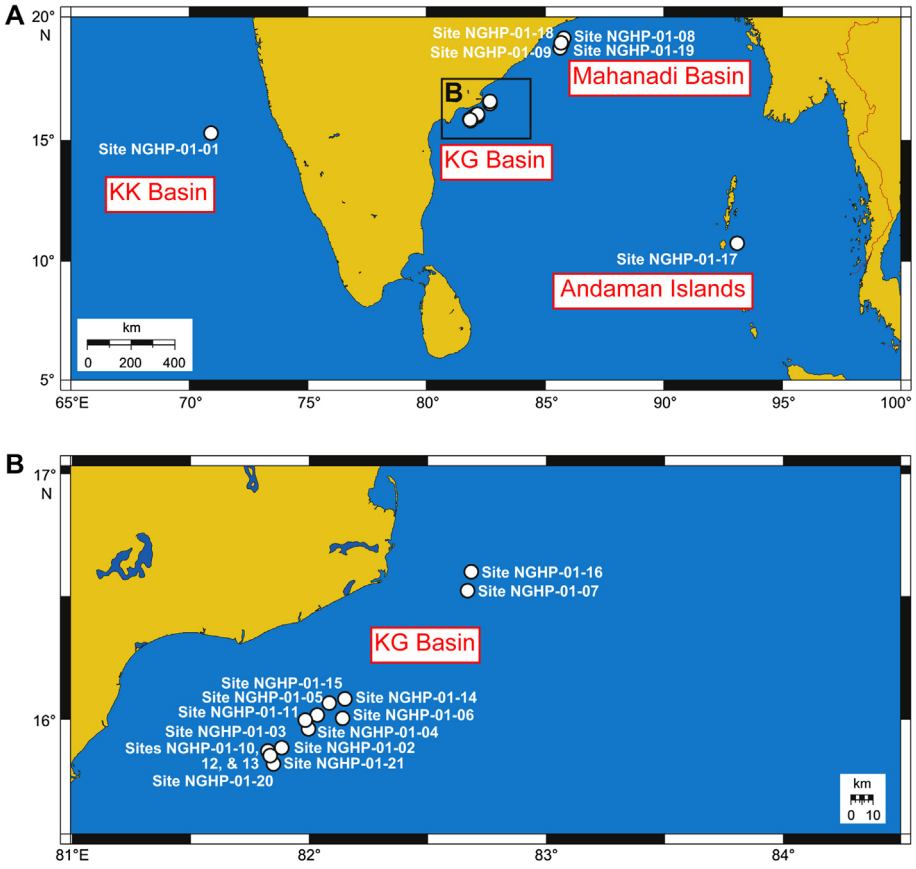

Figure 2. Site location map for the NGHP-01 expedition, including the Kerala-Konkan (KK), Krishna-Godavari (KG), and Mahanadi Basins, and offshore the Andaman Islands. Map "B" shows drill sites occupied in the KG Basin (Collett et al., 2008a).

JOIDES *Resolution* to study the geologic controls on the distribution and characteristics of gas-hydrate deposits (Collett et al., 2008a, 2008b; Kumar et al., 2007). The program drilled 39 holes at 21 sites with a 78% recovery rate for 2850 m of core (Collett et al., 2008a). More than 6000 samples were collected for various analyses, including more than 1800 samples for grain size. Physical properties were measured onboard ship on almost all recovered cores. A select subset of the physical property results from five drilled and cored holes (NGHP-01-1A, -10D, -15A, -17A, and -19A) is presented here and the sites represent four different regions. Summary descriptions of the five holes follow (Collett et al., 2008a): Site NGHP-01-1 is from the Kerala-Konkan (KK) Basin, located on the western continental margin of India in the Arabian Sea. The hydrate-free KK Basin is composed of carbonate-rich pelagic sediment of low organic carbon content, in contrast with sites drilled off the east coast of India. Site NGHP-01-10, located in the Krishna-Godavari Basin, consists mainly of nannofossil-bearing to nannofossil-rich clay-sized grains. Minor silt-sized and little or no sand-sized grains are present. The extensive gas-hydrate deposits (Lee and Collett, 2009a) occur as nodules, disseminated hydrate, fracture fill in shale, and complex, high-angle and horizontal veins (Rees et al., 2011) (Figs. 3A–C, 4). Site NGHP-01-15, also located in the Krishna–Godavari Basin, consists of nannofossil-bearing to nannofossil-rich clay, clay, and silty clay with thicker sand beds than are present in adjacent sites. One sandy zone contained higher gas hydrate pore saturations than surrounding layers and coincided with low infrared temperatures, high resistivity-log values, and porewater chlorinity freshening (Riedel et al., 2011). Site NGHP-01-17, off the Andaman Islands, consists of rapidly deposited nannofossil oozes with varying amounts of foraminifera and siliceous microfossils to a depth of 692 m below the seafloor (mbsf). Although terrigenous sediment content is low, this zone contains hundreds of pyroclastic horizons. Gas hydrate was detected in numerous cm-thick ash beds and ash-rich layers (Rose et al., 2014) from about 250–608 mbsf. This lower depth coincides with the deepest bottom-simulating reflector (BSR) of any site drilled during the NGHP-01 expedition. Hydrate was not visually observed on the catwalk, but was inferred from correlations between infrared (IR) low temperature anomalies, high P-wave velocities, and higher resistivity log values. Site NGHP-01-19, in the Mahanadi Basin, has the most complex lithology observed during NGHP-01. Clays, alternating with a few thin ooze layers, contain biogenic, authigenic, and volcanogenic secondary components. The gas hydrate occurs within the clays as pore- or fracture-filling. Distributions may reach ~10–15% pore saturation within the 25 m of clayey sediment immediately above the BSR at an approximate depth of 205 mbsf, but most occurrences are less than 5% saturation (Collett et al., 2008a).

Supplementary data related to this article can be found online at http://dx.doi.org/10.1016/j.marpetgeo.2014.07.024.

2.1.2. N. Cascadia margin (IODP expedition 311)

The Integrated Ocean Drilling Program (IODP) Expedition 311occupied five sites off Vancouver Island, Canada in 2005. Four of those sites—U1326, U1325, U1327, and U1329—were drilled from seaward to landward locations, respectively. The sites are at different stages of a gas hydrate evolutionary cycle in an accretionary margin (Riedel et al., 2010b). The physical properties of sediments obtained at two of the sites, U1327 and U1329, are reported as part of this study. Significant variability in hydrate

Figure 3. (A) Thin, high-angle gas hydrate lenses in a sediment core recovered from NGHP-01; (B) Partially dissociated core from NGHP-01-10D (see the dissociation process for this core section in the online movie as Fig. 4); (C) Massive gas hydrate nodule from NGHP-01; (D) Gas hydrate layers and nodules from MD02 (Gulf of Mexico); (E) Hydrate-bearing sandstone from Mount Elbert well; (F) Gas hydrate in a gravel layer from Mallik 2L-38. Photos by W. Winters, USGS.

content and its distribution is present between the five holes drilled at Site U1327, where compiled results indicate that gas hydrate saturations in excess of 80% occur in thin sands and silty sand intervals (Riedel et al., 2010b). Site U1329 lies at the eastern limit of gas hydrates. Although free gas may be present below the BSR, infrared scanning and visual observations did not yield any evidence for gas hydrates. The paucity of hydrates at this site is also supported by well-log measurements that lack high velocity and elevated electrical resistivity (ER) (Riedel et al., 2010b).

2.1.3. Hydrate Ridge (ODP Leg 204)

As in the northern Cascadia continental margin, Hydrate Ridge is also a complex, tectonically active accretionary system. Widespread gas hydrate deposits have been recovered during numerous expeditions (e.g., Bohrmann et al., 1998; Suess et al., 1999). We tested sediment from Site 1249, located on the summit of southern Hydrate Ridge, which is a complicated region where centimeter-scale layers of gas hydrate interbedded with soft sediment (Shipboard Scientific Party, 2003) were recovered, along with massive hydrate chunks, thin plates, and nodules (Torres et al., 2002; Trehu et al., 2004).

2.1.4. Gulf of Mexico (MD02) (JIP Leg 1)

In the northern Gulf of Mexico (GoM) multiple processes including rapid sediment accumulation, erosion, hydrocarbon generation, and salt tectonics have set up complex regional fluid-flow regimes and sedimentary structures (Hutchinson et al., 2008b). Numerous studies have examined these and other GOM phenomena, including seeps (MacDonald et al., 2002), complex stratigraphy (Cooper and Hart, 2003), and various interactions between gas hydrates, free gas, porewater chemistry, heat flow, and fluid flow (Boswell et al., 2012; Ruppel et al., 2005).

In 2002, the Institut Polaire Francais, Paul-Emile Victor (IPEV) and the USGS (with USDOE financial support), jointly conducted a cruise (MD02) in four northern Gulf of Mexico continental-slope areas (Tunica Mound, Orca and Pigmy Basins, Bush Hill, and the Mississippi Canyon region) aboard the R/V *Marion Dufresne* to collect giant piston cores and box cores to determine the distribution of gas hydrate away from vents (Lorenson et al., 2002; Winters et al., 2007a; Winters et al., 2007b). We recovered massive gas hydrate (Fig. 3D) in four cores from previously known venting areas in subbottom depths at about 3–9 mbsf, but none was found in adjacent basins. In addition to the sedimentological and physical properties measurements (Winters et al., 2007c), we

made 17 successful passive heat-flow measurements to subbottom depths of 17 m in conjunction with hundreds of pore-water and gas-chemistry measurements (Winters et al., 2007a).

In 2005, the Chevron Joint Industry Project drilled and cored boreholes located in Atwater Valley (AT) and Keathley Canyon (KC) lease blocks to study the occurrence of gas hydrate (Claypool, 2006; Ruppel et al., 2008). Recovered sediment cores were used to characterize and compare bulk physical properties between sites (Winters et al., 2008a).

2.1.5. Blake Ridge (ODP Leg 164)

In 1995, the first Ocean Drilling Program (ODP) study dedicated to gas hydrates was conducted on or near the Cape Fear Diapir (Site 991), at the Blake Ridge Diapir (Site 996), and on the eastern edge of the inner Blake Ridge (Sites 994, 995, and 997) (Paull et al., 1996). The cruise concentrated on Sites 994, 995 and 997, which had penetrations of more than 700 m. Disseminated hydrate was typically recovered in fine-grained sediment whereas rare massive hydrate was retrieved from fractures. More abundant siliceous microfossils in the sediment created larger pore spaces that resulted in increased hydrate content between 185 and 260 mbsf (Kraemer et al., 2000). Winters et al. (2000b) studied the stress history of the Blake Ridge to determine if high sedimentation rates in conjunction with the presence of gas hydrate, which could cement grains, influenced the normal compaction process. Underconsolidation was found at Site 995.

2.2. ARCTIC (Permafrost-related)

2.2.1. North slope. Alaska (Mount Elbert)

Six regional hydrate-bearing sandstone or conglomerate units (typically 3-m to 30-m thick) labeled as “F” (shallowest) through “A” (deepest) are present on the Alaskan North Slope (Collett, 1995, 2002, 2008). In 2007, about 30.5 m of hydrate-bearing sandstone core (Fig. 3E) was recovered in the Mount Elbert well in units D and C that are present below the base of permafrost (see Section 4.2.1).

2.2.2. Mackenzie Delta, Northwest Territories, Canada (Mallik 2L-38 and 5L-38)

Two international research programs were conducted in 1998 and 2002 to study a highly concentrated occurrence of natural gas hydrate in the Canadian Arctic. More than 192 m of core were recovered from depths of 886 m–952 m in 1998 and from 885 m to 1151 m in 2002 (Dallimore and Collett, 2005; Dallimore et al., 1999b). Gas hydrates, with pore saturations of more than 80% at some depths, typically filled sediment voids or coated grains within coarse sand and gravel deposits between 897 and 922 m (Collett et al., 1999; Dallimore et al., 1999a; Winters et al., 1999a) (Fig. 3F).

3. Methods

The methods described here were applied to samples recovered during the NGHP-01 field program. More detail is presented in the Methods section of the Expedition 01 Initial Reports volume (Collett et al., 2008a). Although similar techniques were used during other test programs, some details may be different. Additional information is presented in project-specific references listed in Table 1.

3.1. Infrared imaging

A track-mounted FLIR ThermaCam SC 2000 infrared scanning and recording system, provided by Geotek, Ltd., scanned cores on the catwalk. Temperature-related color images of the scans were displayed on screens above the cores to assist in locating colder hydrate sections (Long et al., 2010) that were quickly removed for additional studies or for preservation in liquid nitrogen.

3.2. Multi-sensor core logging (MSCL)

After 1.5-m-long whole-round core sections were thermally equilibrated to room temperature, they were processed through a Geotek Ltd. Multisensor Core Logger-Standard (MSCL-S) to determine gamma-ray attenuation, bulk density, P-wave velocity, non-contact electrical resistivity, and magnetic susceptibility (Geotek, 2000).

3.3. Thermal conductivity

Thermal conductivity measurements were performed on each 1.5-m-long whole-round core section using a Teka Bolin TK04 (Blum, 1997) single needle probe (von Herzen and Maxwell, 1959) containing a heater wire and calibrated thermistor. All thermal conductivity measurements and other tests performed on split cores (below) were conducted at ambient pressure, not in situ effective stress. Therefore results are relatively consistent, but may differ from field values. However, subsequently performed laboratory tests on whole-round specimens were performed with re-developed effective stress (Section 3.11).

3.4. Core splitting

After thermal conductivity measurements were completed, the core sections were longitudinally split to expose internal sediment surfaces for sedimentologic description on an “archive” half, while the adjacent “working” half had additional testing performed, followed by subsampling. Core sections were wrapped in clear thin plastic wrap to minimize porewater evaporation if additional physical-property testing was not to commence immediately. The splitting process typically was completed within a couple days of recovery, but after any gas hydrates that may have been present dissociated. Split cores were air-conditioned during testing.

3.5. Contact electrical resistivity

A four-pin Wenner array was inserted longitudinally into the surface of the split core about every 10–20 cm in the top of the hole and at greater spacing at depth. The gold-plated pins had a spacing of 2.5 mm and were approximately 3-mm long.

3.6. Contact P-wave velocity

P-wave velocity was measured longitudinally on core sections using a pair of spade-mounted acoustic transducers with resonant frequencies of ~425 kHz. Measurements, which were corrected for temperature, typically could not be successfully performed below the sulfate-methane interface (SMI) because of the disruption caused by gas expansion. As such, these data sets are typically limited to shallow cores at each site.

3.7. Penetrometer and vane strength properties

Pocket penetrometer strength (S_{pp}) tests were performed using a Brainard-Kilman model S-170 (NGHP-01, IODP X311) or a Soiltest model CL-700 (ODP Leg 164) penetrometer. This test is performed by recording the force required to push a spring-loaded probe into a split-core face. It can measure strengths to about 220–250 kPa.

The Torvane® is a hand-held instrument in which a multi-bladed circular disc is inserted ~5 mm into a split-core face. It is operated by rotating a handle connected to the disc through a vertically

oriented spring. The Torvane® strength (S_{tv}) is determined from the torque required to shear the sediment surrounding the disc. It can measure strength to values of 250 kPa.

The vane-shear strength (S_v) was determined with a 12.7-mm high by 12.7-mm diameter vane inserted one vane height into the sediment sample and rotated at a rate of ~90° per minute. Sensitivity (S_t) was determined by S_v/S_r, where S_r is the remolded strength determined after the vane was quickly rotated an additional revolution.

3.8. Index properties

After other physical-property tests were completed, subsamples of the core working half were obtained for water content and grain density. Water content (wc) based on dry sediment mass, was determined according to American Society for Testing and Materials (ASTM) Standard D 2216 (ASTM, 2006) at a drying temperature of 110 °C. Shore-based Atterberg Limits (liquid limit (LL) and plastic limit (PL)) were mainly performed on whole-round core sections according to ASTM Standard D 4318 (ASTM, 2008c) using the three-point method. Unified classification, dry strength, dilatancy, and toughness were described according to ASTM Standard D 2488 (ASTM, 2008a). Grain density was determined using a helium gas pycnometer according to ASTM Standard D 5550 (ASTM, 1997). Porosity and bulk density were calculated from phase relationships assuming saturated pore space (Winters et al., 2007c).

3.9. Grain size

Two methods were mainly used to determine grain-size properties. The vast majority of analyses used a Beckman Coulter™ Laser Diffraction Particle Size Analyzer (LDPSA) Model LS 13 320. Laser-diffraction particle-size analysis gives highly reproducible volume percent results (on small wet sediment samples (<1 g)) in short test times (Kelly et al., 2006).

The second method used a Coulter Counter, whereby a specimen was oven dried at 90 °C to determine component masses and water content. Each specimen was then wet-sieved to separate the coarse (>0.062 mm) and fine (<0.062 mm) fractions. A Coulter Counter electro-resistance multi-channel particle-size analyzer (Poppe et al., 2004) was used on the fine fraction.

Standard relations are used to classify (Shepard, 1954) and report the percent sand, silt, and clay-size grains in the samples (Wentworth, 1929). Skewness is related to the distribution of particles on each side of a grain-size frequency curve, whereas kurtosis is a measure of the steepness in the central portion of the curve. Details of the grain size procedure are provided elsewhere (Poppe et al., 2005).

3.10. Consolidation properties

Back-pressured constant-rate-of-strain consolidation tests were performed in general accordance with ASTM Standard D 4186 (ASTM, 2008b) using a (a) Geocomp LoadTrac II loading frame to apply the loading stress and a Geocomp FlowTracII unit to apply sample pressure, or (b) a high-load-capacity rock mechanics test system modified to perform consolidation testing (Winters et al., 2000b).

Test results are plotted as strain (or void ratio = volume voids/volume solids) versus logarithm of the average vertical effective stress. Typical curves form a straight line, the virgin compression line, at higher stresses. The slope of the virgin line, in terms of strain, is termed the modified compression index ($C_{c\varepsilon}$), and represents how much one-dimensional compression can be expected from a logarithmic cycle of loading. The compression index (C_c), in terms of void ratio, is related to the modified compression index by $C_c = C_{c\varepsilon}(1 + e_o)$, where e_o is the initial void ratio.

Stress history was estimated by comparing the maximum past stress (σ'_{vm}), with the existing in situ vertical effective stress (σ'_{vo}). The preconsolidation stress (p'_c), can be determined from consolidation test results that have a straight virgin line by various graphical techniques (ASTM, 2008b; Casagrande, 1936) and is assumed to equal σ'_{vm}. Two parameters are used to make the σ'_{vm} to σ'_{vo} comparison. The excess effective stress (σ'_e) is $\sigma'_{vm}-\sigma'_{vo}$, whereas the overconsolidation ratio (OCR), is $\sigma'_{vm}/\sigma'_{vo}$. Average effective axial stress and coefficient of consolidation (c_v) were determined according to ASTM D 4186.

3.11. Triaxial strength properties

Triaxial shear tests were performed using a Geocomp LoadTrac II loading frame to apply the loading stress and a Geocomp FlowTracII unit to apply sample pressure (e.g., Marr, 2002) or a rock mechanics system modified to handle hydrate-bearing sediment (Winters et al., 2000b). Triaxial tests simulate in situ conditions by applying an internal pressure that is lower than an external pressure. After consolidation, the difference in pressure develops an effective stress in the sample related to subbottom burial. Vertically loading the sample to 15–20% strain at a constant rate that equalizes pore pressure enables various large-strain properties, such as effective friction angle (φ'), effective cohesion intercept (c'), pore pressure coefficient (A), and failure strain, to be calculated (ASTM, 2010; Bishop and Henkle, 1962).

4. Results and discussion

4.1. NGHP-01 comparisons

Index and geotechnical properties from NGHP-01 are presented here and compared to properties of sediment from other projects in Section 4.2. To illustrate within-hole sediment characteristics and behavior and compare regional trends, physical property and well log results have been combined into composite profiles for five holes from NGHP-01: -1A, -10D, -15A, -17A, and -19A (Figs. 5–9) representing the four main regions drilled during NGHP-01 (Fig. 2). Detailed results from the other projects have been presented in the respective publications listed in Table 1.

Except for Hole NGHP-01-1A, properties, such as S_{pp}/σ'_v, sensitivity, apparent formation factor, and contact P-wave velocity, that exhibit similar behavior in each hole will be discussed as individual groups in Section 4.1.2. Because Atterberg limits, consolidation, and triaxial strength properties are not presented in any of the NGHP-01 property profiles, they will be discussed separately in Section 4.2.

4.1.1. Individual NGHP-01 hole profiles

4.1.1.1. Kerala-Konkan (KK) Basin (Hole NGHP-01-1A). The sediment, typically a nannofossil ooze, is fine grained, typically at the clay-size to very fine silt boundary (Wentworth, 1929) (median: 4.2 μm, Tables 2 and 3, Fig. 10) with only a couple outliers (Fig. 5) in Hole 1A. Median grain size is nearly uniform with depth, decreasing at a statistical rate of 0.11 μm per 100 m (Table 4).

Porosity decreases from 71% (median: 68%) near the top of the hole, at a rate of about 31% per 100 m, but this becomes consistent (regression coefficient (R): 0.86) at a rate of 6.8% per 100 m for the rest of the hole (Tables 5 and 6). In this paper, we use straight-line segments to simplify intra- and inter-well comparisons, whereas others have used exponential or polynomial models to describe porosity versus subbottom depth trends (e.g.,Hamilton, 1976; Torres et al., 2004) (Table 6). This is appropriate for the present

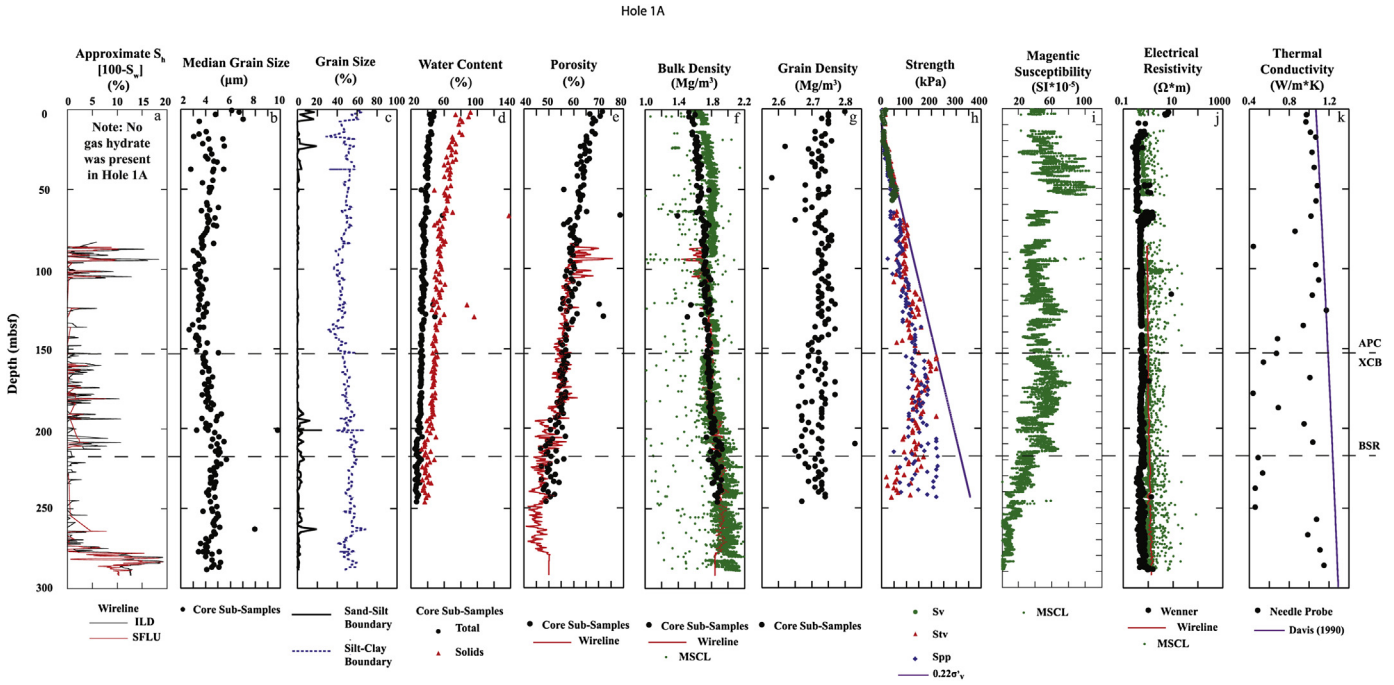

Figure 5. Profiles of sediment properties from Hole NGHP-01-1A including: (a) gas hydrate pore saturation (Sh) determined using wireline logs (Collett et al., 2008a), (b and c) median grain size and percent sand, silt, clay, (d) water content in terms of total and solid specimen masses, (e, f, g) porosity, bulk density, and grain density determined from moisture and density (MAD) specimens, compared to wireline and Multi-Sensor Core Logger (MSCL) measurements, (h) shear strength measurements determined from laboratory mini-vane, Torvane®, and Pocket Penetrometer devices compared to a 0.22 × vertical effective stress line, (i) magnetic susceptibility determined with a Multi-Sensor Core Logger (MSCL) on whole-round core sections, (j) electrical resistivity determined using wireline logs (Collett et al., 2008a), an MSCL on whole-round core sections, and a Wenner array device on longitudinally split core sections, (k) thermal conductivity determined on whole-round cores using a needle probe method. The subbottom depth at which sampling was changed from hydraulically pushed Advance Piston Corer (APC) to rotary Extended Core Barrel (XCB) is important because of its effect on core recovery and disturbance. The estimated depth of the bottom-simulating reflector (BSR) is also shown, however, gas hydrates were not recovered in Hole NGHP-01-1A.

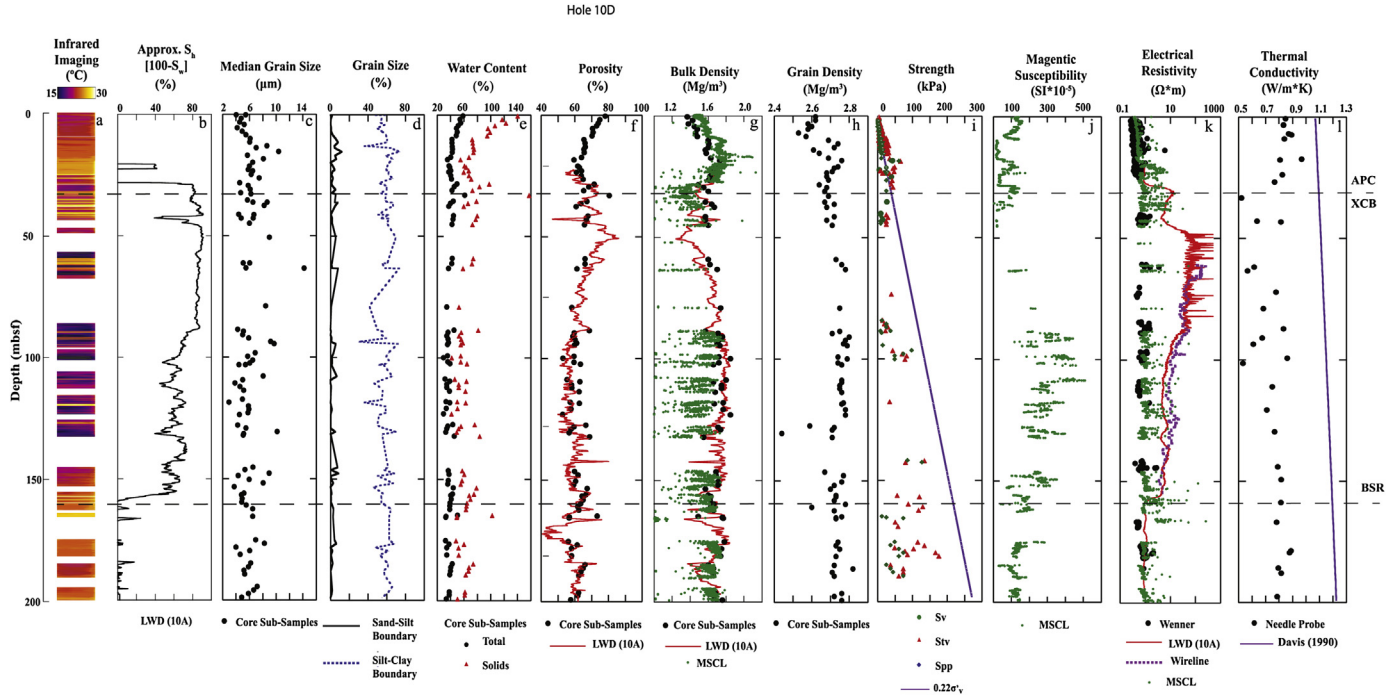

Figure 6. Profiles of sediment properties from Hole NGHP-01-10D including: (a) infrared thermal imaging of discontinuous whole-round cores on the catwalk prior to sample removal, (b) gas hydrate pore saturation (Sh) determined using a logging-while-drilling (LWD) log (Collett et al., 2008a), (c and d) median grain size and percent sand, silt, clay, (e) water content in terms of total and solid specimen masses, (f, g, h) porosity, bulk density, and grain density determined from moisture and density (MAD) specimens, compared to LWD and Multi-Sensor Core Logger (MSCL) measurements, (i) shear strength measurements determined from laboratory mini-vane, Torvane®, and Pocket Penetrometer devices compared to a 0.22 × vertical effective stress line, (j) magnetic susceptibility determined with a Multi-Sensor Core Logger (MSCL) on whole-round core sections, (k) electrical resistivity determined using LWD and wireline logs (Collett et al., 2008a), an MSCL on whole-round core sections, and a Wenner array device on longitudinally split core sections, and (l) thermal conductivity determined on whole-round cores using a needle probe method. The subbottom depth at which sampling was changed from hydraulically pushed Advance Piston Corer (APC) to rotary Extended Core Barrel (XCB) is important because of its effect on core recovery and disturbance. The estimated depth of the bottom-simulating reflector (BSR) is also shown.

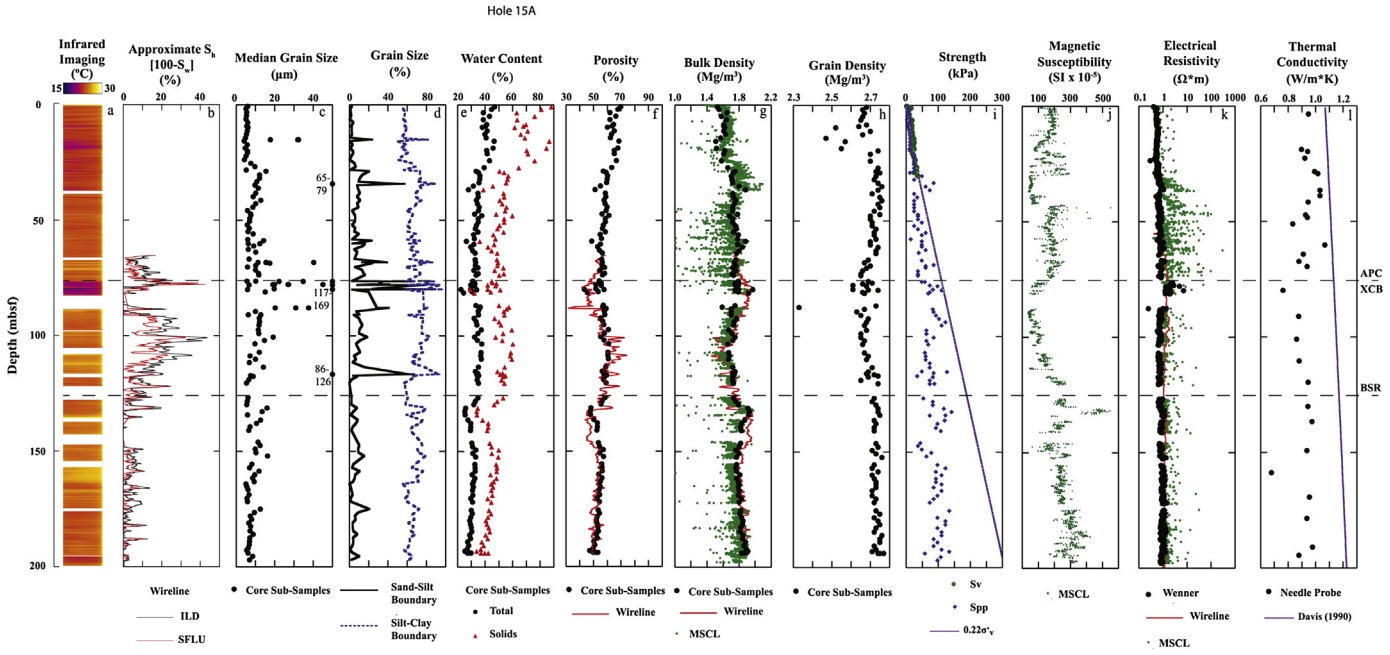

Figure 7. Profiles of sediment properties from Hole NGHP-01-15A including: (a) infrared thermal imaging of discontinuous whole-round cores on the catwalk prior to sample removal, (b) gas hydrate pore saturation (Sh) determined using wireline logs (Collett et al., 2008a), (c and d) median grain size and percent sand, silt, clay, (e) water content in terms of total and solid specimen masses, (f, g, h) porosity, bulk density, and grain density determined from moisture and density (MAD) specimens, compared to wireline and Multi-Sensor Core Logger (MSCL) measurements, (i) shear strength measurements determined from laboratory mini-vane, Torvane®, and Pocket Penetrometer devices compared to a 0.22 × vertical effective stress line, (j) magnetic susceptibility determined with an MSCL on whole-round core sections, (k) electrical resistivity determined using a wireline log (Collett et al., 2008a), an MSCL on whole-round core sections, and a Wenner array device on longitudinally split core sections, and (l) thermal conductivity determined on whole-round cores using a needle probe method. The subbottom depth at which sampling was changed from hydraulically pushed Advance Piston Corer (APC) to rotary Extended Core Barrel (XCB) is important because of its effect on core recovery and disturbance. The estimated depth of the bottom-simulating reflector (BSR) is also shown.

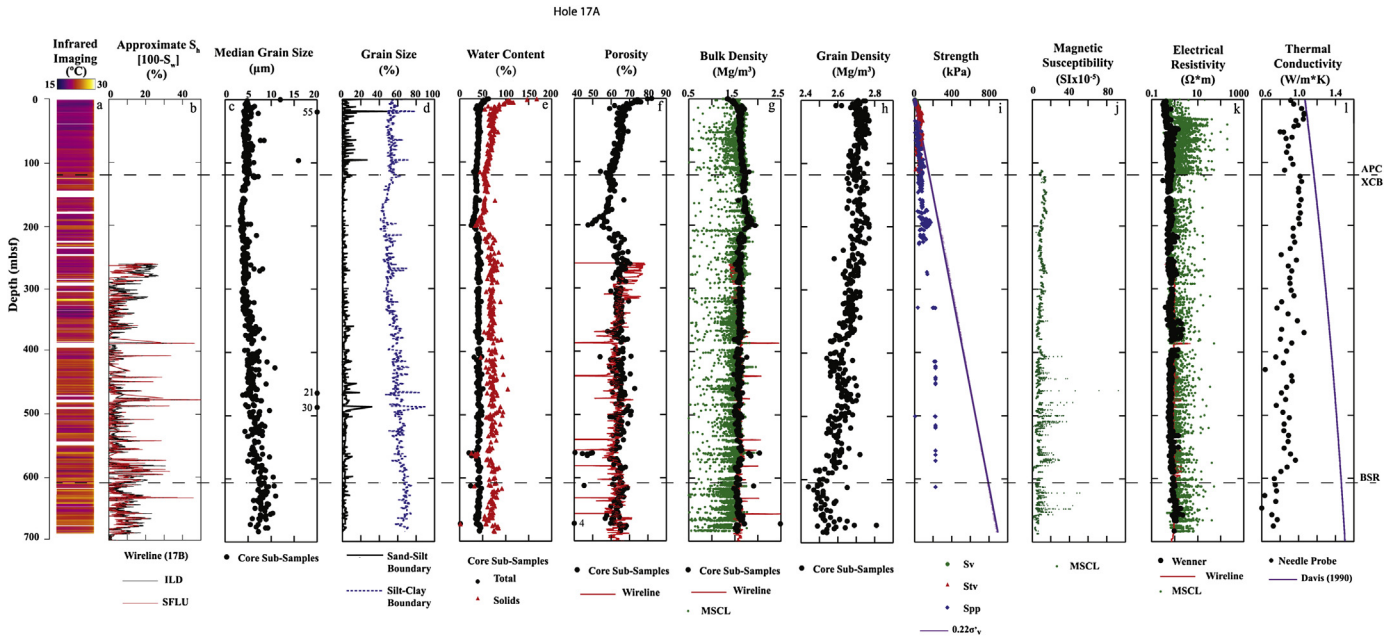

Figure 8. Profiles of sediment properties from Hole NGHP-01-17A including: (a) infrared thermal imaging of discontinuous whole-round cores on the catwalk prior to sample removal, (b) gas hydrate pore saturation (Sh) determined using wireline logs (Collett et al., 2008a), (c and d) median grain size and percent sand, silt, clay, (e) water content in terms of total and solid specimen masses, (f, g, h) porosity, bulk density, and grain density determined from moisture and density (MAD) specimens, compared to wireline and Multi-Sensor Core Logger (MSCL) measurements, (i) shear strength measurements determined from laboratory mini-vane, Torvane®, and Pocket Penetrometer devices compared to a 0.22 × vertical effective stress line, (j) magnetic susceptibility determined with an MSCL on whole-round core sections, (k) electrical resistivity determined using a wireline log (Collett et al., 2008a), an MSCL on whole-round core sections, and a Wenner array device on longitudinally split core sections, and (l) thermal conductivity determined on whole-round cores using a needle probe method. The subbottom depth at which sampling was changed from hydraulically pushed Advance Piston Corer (APC) to rotary Extended Core Barrel (XCB) is important because of its effect on core recovery and disturbance. The estimated depth of the bottom-simulating reflector (BSR) is also shown.

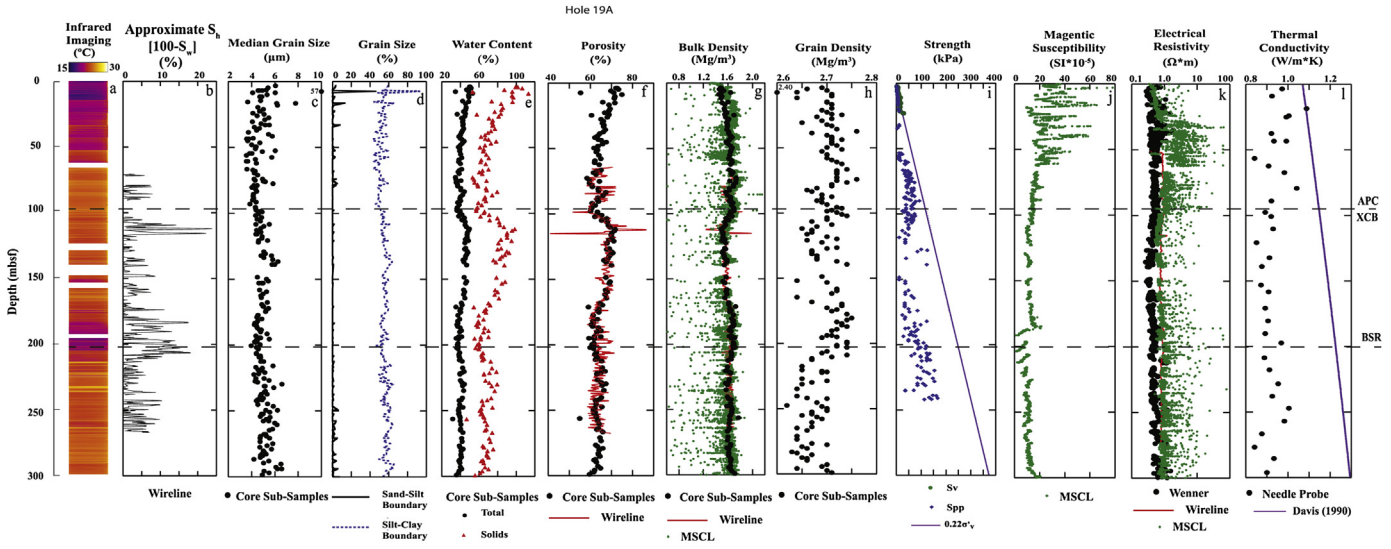

Figure 9. Profiles of sediment properties from Hole NGHP-01-19A including: (a) infrared thermal imaging of discontinuous whole-round cores on the catwalk prior to sample removal, (b) gas hydrate pore saturation (Sh) determined using a wireline log (Collett et al., 2008a), (c and d) median grain size and percent sand, silt, clay, (e) water content in terms of total and solid specimen masses, (f, g, h) porosity, bulk density, and grain density determined from moisture and density (MAD) specimens, compared to wireline and Multi-Sensor Core Logger (MSCL) measurements, (i) shear strength measurements determined from laboratory mini-vane, Torvane®, and Pocket Penetrometer devices compared to a 0.22 × vertical effective stress line, (j) magnetic susceptibility determined with an MSCL on whole-round core sections, (k) electrical resistivity determined using a wireline log (Collett et al., 2008a), an MSCL on whole-round core sections, and a Wenner array device on longitudinally split core sections, and (l) thermal conductivity determined on whole-round cores using a needle probe method. The subbottom depth at which sampling was changed from hydraulically pushed Advance Piston Corer (APC) to rotary Extended Core Barrel (XCB) is important because of its effect on core recovery and disturbance. The estimated depth of the bottom-simulating reflector (BSR) is also shown.

study because straight-line segments facilitate comparison, provide immediate recognition of rate effects, and are very close to more advanced models over discrete depth intervals. In addition, the exponential porosity law may not apply in all instances (Busch, 1989). At Hole NGHP-01-1A, porosity versus depth approximates the trends for deep-sea terrigenous and calcareous sediment (Fig. 11A) (Hamilton, 1976). Assuming saturated conditions with constant grain density, water content and porosity are directly related, while bulk density is inversely related (Fig. 5). Grain density has a median value of 2.73 Mg/m^3 (Table 3) and is essentially constant with depth (Table 4; R is small indicating grain density varies little with depth – No change with depth would have an $R = 0$). Visual examination of the profiles indicates that sediment subsample, MSCL, and well-log results overall compare favorably except for an offset in the bulk density between subsample and MSCL in the top of the hole (Fig. 5).

Because mini-vane, Pocket Penetrometer, and Torvane® strength results agree very well for Hole NGHP-01-1A (Fig. 11B), only Pocket Penetrometer results are shown for the other holes (Fig. 11C). S_{pp}/σ'_v at the top of Hole NGHP-01-1A exhibits pseudo-overconsolidated behavior prevalent in many fine-grained sediments where electrical forces at shallow subbottom depth influence compaction more than gravitational forces (Francisca et al., 2005). Variations in clay mineralogy and sedimentation rates affect compaction patterns at low overburden stresses (Busch, 1989). This upper zone has sediment characteristics (high water content, etc.) similar to a modern depositional environment rather than the stiff behavior characteristic of truly heavily overconsolidated material. Below this upper zone, S_{pp}/σ'_v starts at about 0.12 and very slowly decreases with depth (Table 4). Undrained strength/σ'_v ratios vary widely from 0.09 to 0.35 (Bowles, 1979) and 0.16 to 0.4 (Hunt, 1984) for normally consolidated clays. Although a number of correlations relate the ratio to both plasticity index and liquidity index (Holtz and Kovacs, 1981), Mesri (1975, 1989) found that field undrained shear strength/σ'_v equals 0.22 for soft clays regardless of plasticity. Although laboratory mini-vane shear tests on split cores are performed without effective stress developed by more advanced test methods, strength/σ'_v values approximate 0.22 in the upper part of Hole NGHP-01-1A. The implication is that these sediments have not been heavily overconsolidated due to geologic mass wasting or other events. However, strength/σ'_v values increasingly diverge from 0.22 with depth as a result of coring disturbance (below the APC/XCB boundary) or penetrometer measurement limitations (220–250 kPa, Section 3.7) (Fig. 5). APC/XCB boundary refers to the subbottom depth at which drilling changed from the hydraulically-pushed Advanced Piston Corer tool, used in shallow, weaker sediment, to the Extended Core Barrel tool that utilizes rotary drilling in stiffer sediment.

Vane shear strength sensitivity (peak/remolded strength) is between 3 and 4 near the top of the hole and the best fit trend varies little with depth (Table 4, Fig. 11D). Values range from 2 (insensitive) to 7 (sensitive) (Hunt, 1984), however, they are much lower and therefore more stable in some circumstances, than "quick" clays that lose almost all of their strength after remolding.

The magnetic susceptibility of a material is related to its response (number of dipole orientations) to an external magnetic field. Some materials enhance the applied field and are positive, whereas the presence of other materials reduce the effect of the field and are negative (for example, water). Although dimensionless, the SI system is now used more extensively than the older cgs system of measurement. Sediments can vary from 10^{-5} SI all the way to ~1 SI for highly magnetic minerals (for example, magnetite) (Clark and Emerson, 1991). The magnetic signature of sediment can also be the result of original detrital material and changes induced in iron minerals caused by hydrate formation (Esteban et al., 2008). Magnetic susceptibility has some variability down hole, but values are on the low side in Hole NGHP-01-1A reflecting the predominant biogenic nature of the sediment and lack of magnetic minerals. The median value for the hole is $41^{*}10^{-5}$ SI (Table 3) and trends lower with depth (Table 4, Fig. 5).

Electrical resistivity measurements on core subsamples, MSCL values, and well-log results are in overall agreement (Fig. 5),

Table 2
Statistics of individual grain-size analyses from the NGHP-01 expedition, organized by overall project and region. A separate set of analyses was performed on 23 samples thought to contain gas hydrate that were infrared scanned for temperature anomalies at sea.

	Sand (%)	Silt (%)	Clay-size (%)	Mean grain size (□m)	D_{90} (μm)	D_{50} (μm)	D_{10} (μm)	Mean/Median	Mode	Stand. Dev. (μm)	Variance (μm^2)	Skewness	Kurtosis
All Holes													
min	0.00	0.00	2.79	1.65	2.29	1.86	0.77	0.49	2.11	1.35	1.83	−2.63	−1.26
max	88.75	74.36	100.0	129.11	750.76	168.64	53.96	1.62	245.2	7.40	54.71	0.94	12.99
mean	3.61	54.07	42.28	6.88	36.89	6.89	1.46	1.05	8.62	3.22	10.80	0.14	−0.56
median	1.47	54.44	43.16	5.70	28.52	5.29	1.32	1.05	4.88	3.17	10.09	0.14	−0.66
stnd dev	7.09	7.10	9.18	6.68	40.20	9.35	1.72	0.08	19.80	0.58	4.17	0.23	0.58
no. tests	2063	2063	2063	2063	2043	2063	2043	2063	2043	2063	2043	2063	2063
Andaman Islands													
min	0.00	0.00	10.69	1.65	2.29	1.86	0.96	0.65	2.11	1.35	1.83	−0.61	−1.26
max	48.13	74.36	100.0	35.98	372.46	55.37	3.95	1.40	245.2	7.40	54.71	0.67	0.95
mean	3.15	53.50	43.35	6.34	36.78	5.80	1.38	1.12	4.95	3.33	11.28	0.23	−0.66
median	2.19	52.52	44.32	5.95	34.53	5.10	1.33	1.13	3.06	3.28	10.76	0.26	−0.72
stnd dev	4.07	7.17	8.08	2.34	22.25	3.06	0.24	0.08	12.94	0.44	3.46	0.20	0.25
no. tests	542	542	542	542	542	542	542	542	542	542	542	542	542
KG Basin													
min	0.00	8.46	2.79	2.67	9.01	2.43	0.77	0.49	2.11	1.39	5.86	−2.63	−1.19
max	88.75	74.04	79.93	129.11	750.76	168.64	53.96	1.27	223.4	6.47	41.81	0.51	7.75
mean	5.40	55.79	38.75	8.30	46.58	8.73	1.57	1.02	13.08	3.44	12.30	0.05	−0.68
median	2.60	56.52	39.33	6.50	33.46	6.23	1.33	1.03	5.35	3.35	11.26	0.07	−0.75
stnd dev	9.29	7.23	9.58	9.30	53.26	13.14	2.51	0.08	26.48	0.59	4.41	0.24	0.54
no. tests	961	961	961	961	948	961	948	961	948	961	948	961	961
KK Basin													
min	0.00	25.15	31.47	2.90	7.75	2.70	0.91	0.85	2.11	1.45	5.19	−0.95	−1.01
max	23.99	58.18	71.47	11.03	174.48	8.83	1.78	1.62	7.08	5.44	29.55	0.84	5.57
mean	1.69	47.86	50.42	4.47	20.29	4.30	1.15	1.04	4.53	2.84	8.36	0.28	0.00
median	0.60	48.69	50.21	4.28	15.40	4.20	1.14	1.03	4.88	2.73	7.50	0.28	−0.09
stnd dev	3.40	5.54	6.63	1.11	19.83	0.85	0.11	0.09	1.30	0.48	3.28	0.22	0.60
no. tests	186	186	186	186	184	186	184	186	184	186	184	186	186
Mahanadi Basin													
min	0.00	20.63	7.19	3.69	12.77	3.42	1.10	0.69	2.54	1.35	5.01	−1.64	−0.83
max	42.61	67.87	76.01	39.71	134.86	57.15	6.12	1.21	105.9	4.78	22.81	0.94	12.99
mean	0.63	53.56	45.76	5.20	20.47	5.04	1.44	1.04	4.60	2.70	7.44	0.15	−0.40
median	0.00	53.87	45.58	4.94	18.34	4.77	1.41	1.04	4.44	2.67	7.15	0.14	−0.49
stnd dev	2.60	5.21	5.84	2.01	9.73	2.84	0.30	0.04	5.37	0.32	1.75	0.18	0.76
no. tests	374	374	374	374	369	374	369	374	369	374	369	374	374
Infrared Scanned Hydrate-Bearing SedimenT													
min	0.17	17.09	5.46	4.07	12.55	3.70	1.07	0.64	2.54	2.39	5.70	−1.59	−1.03
max	77.45	68.76	54.92	101.53	306.16	159.06	12.21	1.16	203.5	4.68	21.92	0.43	2.29
mean	8.60	53.19	38.20	11.88	53.13	14.77	1.94	0.99	20.80	3.44	12.24	0.02	−0.35
median	2.73	53.51	39.94	6.76	34.75	6.30	1.36	1.02	4.88	3.32	11.05	0.16	−0.65
stndev	16.28	9.97	13.25	20.17	61.36	32.13	2.35	0.13	42.05	0.65	4.51	0.45	0.71
no. tests	23	23	23	23	23	23	23	23	23	23	23	23	23

although slight offsets are present. For example, Wenner measurements on core sediment typically are lower than MSCL values (Table 3) because they are made on smaller sections of core that may be more homogeneous than those sampled by the MSCL. In this regard, lower MSCL values, that are less affected by discontinuities in the sediment, are more valid than higher values. Low well-log electrical resistivity throughout the hole reflects the lack of in situ hydrate. Median values for Wenner, MSCL, and well-log measurements are 0.52, 0.82, and 1.03 Ωm (Table 3), respectively, within the range for laboratory and in situ values found by Boyce (1968). Statistically, all measurements trend slightly higher with subbottom depth (Table 4).

The apparent formation factor, which relates resistivity of saturated sediment to that of the pore fluid, provides insights into the interrelationships between the solid and void spaces in the sediment and can be used to interpret relative flow through porous media. Normalizing the Wenner resistivity measurements to those of seawater produced a median value of 2.6 (Table 3) that increases with depth (Table 4, Fig. 11E). This value is within the range of 1.57–3.70 reported by Boyce (1968).

Thermal conductivity is quite variable and is lower than on the northern Cascadia margin (Davis et al., 1990), especially below the APC/XCB boundary (Fig. 5), perhaps reflecting gas expansion and rotary-core disturbance. Other effects of coring and different test methods on sediment from the Cascadia accretionary prism may also contribute to the difference. Median thermal conductivity is 1.0 W/(m*K) (Table 3) and trends along the Davis et al. (1990) relation if only larger values are considered. Although recovery of piston (APC) cores is related to a complex set of sediment properties including shear strength, grain size, porosity, and density, side-by-side comparison of piston and rotary cores has demonstrated the improved quality of piston cores. Rotary coring can produce excellent recovery in certain sediment types (chalk and some sandstones and limestones), but can be very erratic in other materials (clays and loose sands) (Huey, 2009). Because the accuracy of sediment properties is directly related to core quality, typically testing APC cores is preferred to XCB cores for most measured physical properties.

Median contact P-wave velocity is 1.51 km/s (Table 3) and slightly increases with depth (Table 4). This value is close to that of seawater, reflecting the high porosity of the sediment and the lack of confinement during testing (Tobin et al., 1995). Because of the lack of interstitial gas in Hole NGHP-01-1A measurements were able to be made below 40 mbsf (Fig. 11F) (Collett et al., 2008a).

Table 3
Reservoir, drilling operations, sediment core, and well log information and statistics for five holes representative of the four major regions drilled during NGHP-01. APC/XCB depth refers to the subbottom depth at which drilling changed from the hydraulically-pushed Advanced Piston Corer tool, used in shallow weaker sediment, to the Extended Core Barrel tool that utilizes rotary drilling in stronger sediment types.

Region	Hole	Dominant sediment type (Collett et al., 2008b)	Hydrate reservoir classification (Collett et al., 2008b)	APC/XCB depth (mbsf)	Approximate BSR depth (mbsf) (Collett et al., 2008b)		Approx hydrate saturation (%)	Median grain size (μm)	Grain density (Mg/m^3)	Magnetic susceptibility ($SI*10^{-5}$)	Electrical resistivity (Wenner) (Ω m)	Electrical resistivity (MSCL) (Ω m)	Electrical resistivity (LWD) (Ω m)	Electrical resistivity (wireline) (Ω m)	Thermal conductivity (W/m K)	Vane shear strength sensitivity	PP strength /σ'v	Apparent formation factor	Velocity (contact) (km/s)
KK basin	1A	Carbonate Oozes	None	152.8	None ((217))	Depth range (mbsf)	83–214 (ILD); 86-213 (SFLU)	1–288	2–246	1–289	2–289	1–289	–	85–292	3–286	1–57	2–243	9–289	1–41
						Median	2.75//2.01	4.20	2.73	40.99	0.52	0.82	–	1.03	1.00	3.15	0.13	2.60	1.51
						Mean	3.81//2.95	4.33	2.72	41.72	0.59	0.97	–	1.09	0.88	3.39	0.12	2.70	1.51
						Std Dev	3.51//2.71	0.92	0.03	56.57	0.55	1.25	–	0.14	0.24	1.11	0.05	0.77	0.02
KG Basin	10D	Clay/Silt	Fracture	32.6	160	Depth range (mbsf)	28-159 (LWD 10A)	0–199	0–199	0–199	2–146	0–199	48–155// 160–197	61–155	1–198 (10B, 10D, 12A)	2–35	2–189	2–186	0–14
						Median	71.61	5.81	2.72	128.22	0.54	0.88	8.31//0.92	12.22	0.80	3.10	0.11	2.69	1.49
						Mean	71.29	5.96	2.72	156.04	0.65	1.71	35.11//0.95	26.95	0.77	3.19	0.12	3.19	1.49
						Std Dev	15.28	1.48	0.06	107.42	0.48	6.74	68.51//0.09	36.99	0.11	0.91	0.09	1.89	0.01
KG Basin	15A	Clay with Silt/Sand Beds	Silt/Sand	76.1	126	Depth range (mbsf)	ILD//SFLU 68–126	No outliers //23 outliers only 1-197// 15–117	1–194	–	0–198	0–198	–	55–126// 126–201	4–195	0–30	1–193	0–198	1–30
						Median	17.14// 9.84	7.67// 65.00	2.71	–	0.78	1.13	–	1.29//1.18	0.94	2.60	0.11	3.88	1.50
						Mean	17.37// 10.98	9.06// 78.42	2.70	–	0.83	1.97	–	1.37//1.20	0.93	2.68	0.14	4.09	1.51
						Std Dev	8.14//7.54	3.68// 52.37	0.06	–	0.40	6.84	–	0.31//0.09	0.08	0.49	0.11	1.45	0.02
Andaman Islands	17A	Clay/Silt with Volcanic Ash Beds	Silt/Ash	118.5	608	Depth range (mbsf)	ILD//SFLU 261–608 (17B)	No outliers// 4 outliers only 0–684// 19–487	0–684	–	3–683	0–684	–	261–608// 608–719	2–676	1–18	3–198	3–683	0–24
						Median	5.65//5.13	5.09// 31.99	2.67	–	0.66	0.87	–	0.95//0.90	0.90	2.80	0.10	3.28	1.51
						Mean	7.97//7.66	5.56// 35.11	2.66	–	0.69	1.55	–	0.99//0.90	0.89	3.08	0.11	3.43	1.51
						Std Dev	6.87//8.15	1.62// 12.59	0.07	–	0.21	4.15	–	0.22//0.10	0.10	0.87	0.06	1.04	0.02
Mahanadi Basin	19A	Clay with Silt/Sand Beds	Silt/Sand	98.3	205	Depth range (mbsf)	71–205 (19B)	No outliers// 1 outlier only 3–300//7	4–300	0–301	2–300	0–301	–	51–205// 205–280	3–296	3–23	3–242	2–300	3–23
						Median	3.28	4.78// 57.15	2.7	13.02	0.49	0.94	–	0.86//0.81	0.92	3.50	0.09	2.45	1.48
						Mean	4.93	4.87// 57.15	2.69	15.91	0.53	1.87	–	0.86//0.81	0.93	3.66	0.09	2.67	1.48
						Std Dev	4.60	0.63//-	0.04	9.17	0.18	4.64	–	0.09//0.03	0.06	0.97	0.04	0.92	0.01

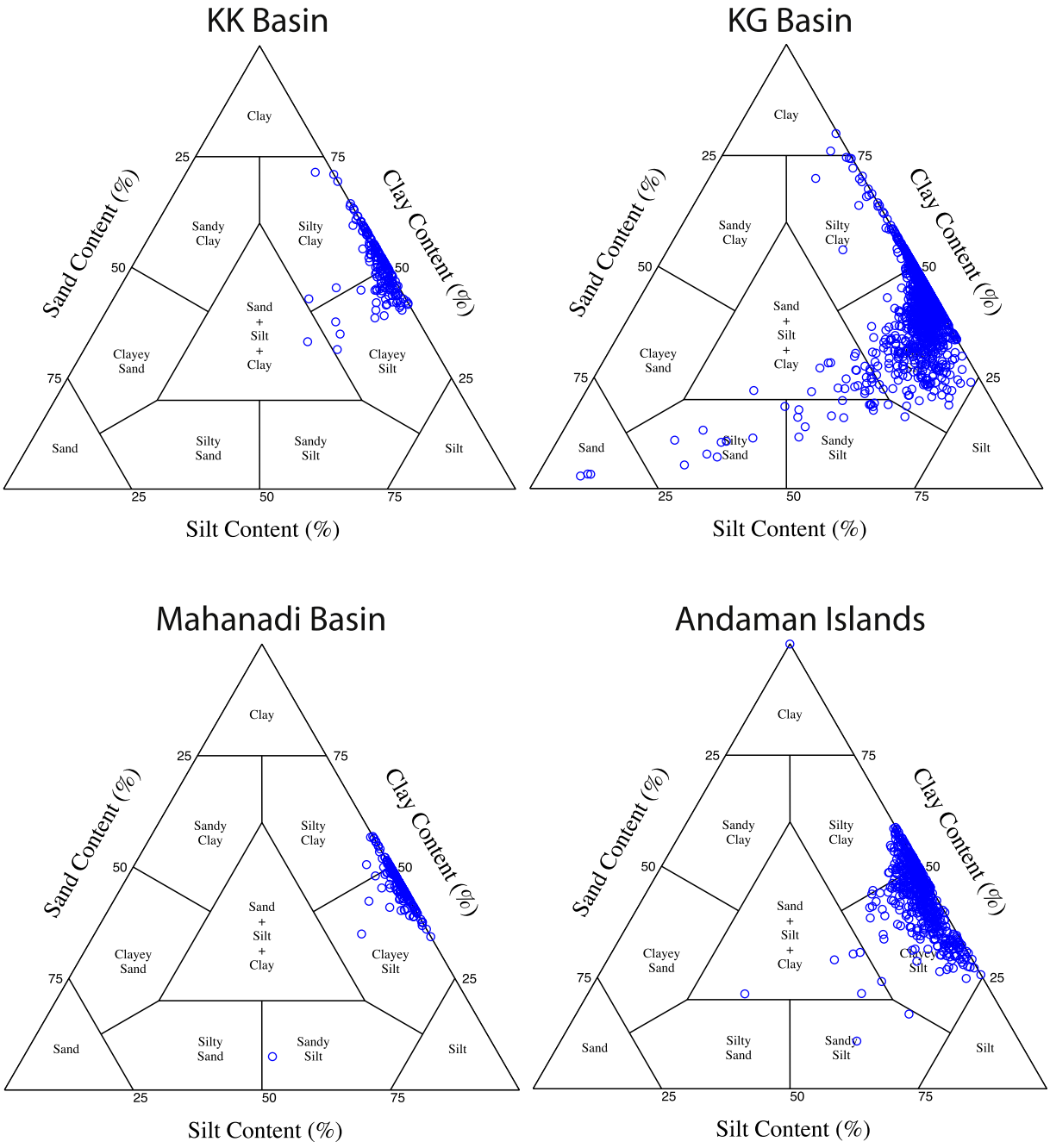

Figure 10. Ternary grain-size plots for more than 2000 analyses from the NGHP-01 expedition.

4.1.1.2. Krishna–Godavari (KG) basin

4.1.1.2.1. Hole NGHP-01-10D. Lithostratigraphically, Hole NGHP-01-10D is classified mainly as nannofossil-bearing to nannofossil-rich clay (Collett et al., 2008a). The sediment in the KG basin has a median grain size of 6.2 μm (very-fine silt according to Wentworth (1929)) (Table 2). Grain size of Hole NGHP-01-10D is slightly finer with a median grain size of 5.8 μm (Table 3, Fig. 6). Median grain size varies from about 2 to 14 μm (Fig. 6) and trends slightly finer with depth, decreasing at a statistical rate of 0.22 μm per 100 m (Table 4). Although gas hydrate saturation is the highest in this hole (median S_h: 72% from 28 to 159 mbsf, Table 3), median grain sizes are relatively small (Fig. 6). An infrared image of core NGHP-01-10D-10X shows a 14 °C temperature difference between the warmest and coolest sediments (Fig. 12). This temperature difference results from the gas hydrate dissociation behavior shown in Fig. 4. Note that some core sections were not recovered so measurements were not performed at all subbottom depths.

Porosity decreases from 78% near the seafloor, at a rate of about 66% per 100 m, in the upper 24 mbsf of the hole (Table 6), but this is greatly reduced to 3% per 100 m in the rest of the hole. Although grain size appears to be uniform, a number of property trends change near the APC/XCB boundary (Fig. 6). These include porosity (and hence water content and bulk density), grain density, and strength. Magnetic susceptibility, electrical resistivity, and thermal conductivity also appear to change trend near that depth. There is an erratic water content/porosity value nearby, possibly related to sample disturbance. Hamilton's (1976) data sets for terrigenous and calcareous deep-sea sediments plot through the center of the Hole

Table 4
Trends in physical property profile data for five holes drilled during NGHP-01. Typically, straight-line fits were used when possible to simplify the comparison process. Note that the regression coefficient (R) for a vertical line is equal to "0.00" and does not necessarily represent scatter in the data, it indicates that a particular property value does not correspond to an individual subbottom depth.

Region	Hole	Hole	Approx hydrate saturation (%)	Median grain size (μm)	Grain density (Mg/m^3)	Magnetic susceptibility ($SI*10^{-5}$)	Electrical resistivity (Wenner) (Ω m)	Electrical resistivity (MSCL) (Ω m)	Electrical resistivity (LWD) (Ω m)	Electrical resistivity (wireline) (Ω m)	Thermal conductivity (W/m K)	Vane shear strength sensitivity	PP strength/σ'v	Apparent formation factor	Velocity (contact)
		Depth range (mbsf)	Sh = (R)	MGS = (R)	GD = (R)	MS = (R)	ER = (R)	ER = (R)	ER = (R)	ER = (R)	ER = (R)	St = (R)	PP/σ'v = (R)	AFF = (R)	Vp ($km\ s^{-1}$) = (R)
KK basin	1A	Depth range (mbsf)	83–214 (ILD); 86–213 (SFLU)	1–288	2–246	1–289	9–289	1–289	–	85–292	3–286	2–57	14–243	9–289	1–41
			6.32– 0.022D (0.25) (ILD); 5.94– 0.027D (0.42) (SFLU)	4.17 + 0.0011D (0.09)	2.73 -0.000069D (0.16)	47.35- 0.11D (0.18)	0.46 + 0.00053D (0.28)	0.39 + 0.0032D (0.21)	–	0.70 + 0.0021D (0.87)	1.00 − 0.00083D (0.30)	3.58 -0.006D (0.10)	0.12 -0.000017D (0.04)	2.29 + 0.0027D (0.28)	1.51 + 0.00026D (0.15)
KG Basin	10D	Depth range (mbsf)	29–152 (LWD 10A)	0–199	0–199	0–199	2–146	0–199	48–155	61–155	1–198 (10B, 10D, 12A)	2–35	11–189	1–186	0–14
			97.4– 0.27D (0.74)	6.17– 0.0022D (0.09)	2.67 + 0.00047D (0.52)	0.24 + 4.85D- 0.022D^2 (0.75)	0.52 + 0.0023D (0.29)	0.80 + 0.0017D (0.02)	440.13* e^(-0.0330D) (0.57)	471.09* e^(-0.0314D) (0.81)	0.77 - 0.000014D (0.01)	4.00 -0.062D (0.61)	0.19 -0.00091D (0.71)	2.50 + 0.012D (Holes 10B, 10D, 12A) (0.39)	1.48 + 0.0018D (0.89)
KG Basin	15A	Depth range (mbsf)	68–126	1-194	1–194	–	0–198	0–198	–	55–201	4–195	1–30	11–193	0–198	1–30
			10.94 + 0.065D (0.14) (ILD); 12.25– 0.013D (0.03) (SFLU)	8.94 + 0.0012D (0.02) (<20 μm); 42.67 + 0.49D (0.26) (>20 μm); 22.86– 0.038D (0.06) (complete);	2.67 + 0.00034D (0.34)	–	0.64 + 0.0020D (0.30)	1.18- 0.0021D (0.03)	–	1.55 - 0.0021D (0.36)	0.95 - 0.00034D (0.25)	2.92 -0.016D (0.32)	0.17 -0.00055D (0.51)	3.13 + 0.010D (0.43)	1.49 + 0.0014D (0.74)
Andaman Islands	17A	Depth range (mbsf)	261–608 (17B)	0–684	0–684	–	3–683	0–684	–	261–719	2–676	1–18	11–198	3–683	0–24
			9.43– 0.0083D (0.12) (ILD); 2.70 + 0.0020D (0.03) (SFLU)	4.22 + 0.0048D (0.29)	2.74 − 0.00027D (0.81)	–	0.53 + 0.00055D (0.51)	0.96- 0.00057D (0.04)	–	1.04 - 0.00014D (0.09)	0.99 - 0.00033D (0.65)	3.35 -0.028D (0.17)	0.17 -0.00069D (0.66)	2.64 + 0.0027D (0.51)	1.48 + 0.0025D (0.91)
Mahanadi Basin	19A	Depth range (mbsf)	71–205 (19B)	3–300	4–301	0–301	2–300	0–301	–	51–280	3–296	3–23	10–242	2–300	3–23
			−2.91 + 0.04 (0.38)	4.58 + 0.0019D (0.26) (with 57 μm outlier rmvd); 5.40– 0.0020D (0.05) (with outlier)	2.71 - 0.00011D (0.34) (outlier rmvd)	32.88- 0.24D + 0.00058D ^2 (0.76)	0.48 + 0.00038D (0.18)	1.28- 0.0024D (0.06)	–	0.88 - 0.00022D (0.18)	0.96 - 0.00021D (0.33)	3.90 -0.019D (0.12)	0.10 -0.00015D (0.29)	2.42 + 0.0019D (0.18)	1.47 + 0.00072D (0.49)

Table 5
Median and mean porosity values for five representative holes drilled during NGHP-01. To simplify comparison between holes, the porosity profiles were partitioned into down-hole "Sections." The upper sediment in all holes is characterized by high-porosity values.

Region	Hole		Porosity (%)				
			Section 1	Section 2	Section 3	Section 4	Section 5
KK basin	01A	Depth range (mbsf)	0–11	11-246			
		Median	68.27	57.12			
		Mean	68.76	57.68			
		Std dev	1.77	5.36			
KG Basin	10D	Depth range (mbsf)	0-24	24-199			
		Median	65.89	61.92			
		Mean	67.43	62.36			
		Std dev	5.12	4.80			
KG Basin	15A	Depth range (mbsf)	0–3	3-194			
		Median	68.74	56.35			
		Mean	68.74	56.42			
		Std dev	1.02	4.48			
Andaman Islands	17A	Depth range (mbsf)	0–9	9-200	200–684		
		Median	73.99	63.62	64.27		
		Mean	74.50	62.68	63.70		
		Std dev	3.50	4.11	4.01		
Mahanadi Basin	19A	Depth range (mbsf)	0–15	15-100	100–115	115–185	185–300
		Median	71.51	63.78	68.25	67.68	63.13
		Mean	69.84	64.10	67.95	66.67	63.18
		Std dev	5.33	2.80	2.82	3.25	2.02

NGHP-01-10D porosity data, although there is some scatter in the NGHP-01-10D data (Fig. 11A). Grain density has a median value of 2.72 Mg/m^3 (Table 3) and increases at a statistical rate of 0.047 Mg/m^3 per 100 m (Table 4).

Magnetic susceptibility begins low near the seafloor, increases throughout the zone containing gas hydrate and slowly decreases to the bottom of the hole (Fig. 6). Median magnetic susceptibility is 128×10^{-5} SI for the hole (Table 3). The wide range in measured values indicates that primary and secondary magnetic minerals are variably present down hole (Collett et al., 2008a).

Sediment subsample, MSCL, and well-log results overall compare favorably except for an offset in the well-log ER plot, which is a result of high in situ gas hydrate pore saturation (Fig. 6). Median values for Wenner and MSCL electrical resistivity measured on core sections without gas hydrate are 0.54 and 0.88 Ω*m (Table 3), respectively, and increase with depth (Table 4). Median LWD and wireline-log measurements are 8.3 and 12.2 Ω*m, respectively, in the hydrate bearing zone to 155 mbsf (Table 3). Below that zone, median LWD ER is 0.92 Ω*m (Table 3), just slightly higher than the median for MSCL measurements.

Thermal conductivity is nearly constant with depth (Table 4, Fig. 6). With a median value of 0.8 W/(m*K), it is lower than on the northern Cascadia margin (Davis et al., 1990). Values are somewhat lower below the APC/XCB boundary (Fig. 6), perhaps reflecting gas expansion and rotary-core disturbance.

4.1.1.2.2. Hole NGHP-01-15A. Site NGHP-01-15 (also located in the KG Basin), consists of nannofossil-rich and -bearing clay with more frequent and thicker sand beds than at adjacent sites (Collett et al., 2008a). The larger median grain sizes correlate with higher in situ gas hydrate pore saturations and thus low temperature infrared anomalies (Fig. 7). Overall, the coarser-grained sediment samples have a median grain size of 65 μm (very fine sand, Wentworth (1929)). However, the coarsest sample has a median grain size of 169 μm (fine sand) (Fig. 7). The median grain size of sediment overlying and beneath the coarser sections in Hole NGHP-01-15A (7.7 μm) is only slightly larger than the median size for the entire basin (6.2 μm) (Tables 2 and 3). Without the coarse fraction (>20 μm), median grain size statistically increases 0.12 μm per 100 m of depth (Table 4). These results are in agreement with Riedel et al. (2011), who describes a 5–8 m thick sandier section, in Hole NGHP-01-15A, that had 20–40% gas hydrate pore saturation and is bounded by a fault that may act as a conduit for gas migration into the hydrate stability zone in this hole. This section is part of a coarser-grained, 10-km-long, channel-levee system that was covered by a finer-grained seal (Riedel et al., 2011).

Porosity decreases fairly uniformly at a rate of 5.0% per 100 m from a high of 70% at the top of the hole to 43% at the bottom of the hole (Table 6), except just below the APC/XCB boundary and the BSR (Fig. 7). Interestingly, all the porosity versus depth data from Hole 15A plot above and subparallel to Hamilton's (1976) data sets for terrigenous and calcareous deep-sea sediments (Fig. 11A) meaning that the sediment composition and environmental conditions have produced a more compacted material with lower porosity. The median value for grain density is 2.71 Mg/m^3 and increases

Table 6
Trends in porosity (n) (compaction) profile data for five holes drilled during NGHP-01. Straight-line fits were used to simplify the comparison process. Note that a regression coefficient (R) for a vertical line is equal to "0.00" and does not necessarily represent scatter in the data, it indicates that a particular porosity value does not correspond to an individual subbottom depth.

Region	Hole	Section	1	2	3	4	5
			n= (R)	n= (R)	n= (R)	n= (R)	n= (R)
KK basin	01A	Depth range (mbsf)	0–11	11-246			
			70.40–0.306D (0.44)	66.51–0.068D (0.86)			
KG Basin	10D	Depth range (mbsf)	0–24	24-199			
			75.44–0.658D (0.94)	65.86–0.030D (0.33)			
KG Basin	15A	Depth range (mbsf)	0–3	3-194			
			71.22–1.880D (1.00)	61.27–0.050D (0.63)			
Andaman Islands	17A	Depth range (mbsf)	0–9	9-200	200–684		
			79.22–1.087D (0.84)	67.77–0.063D (0.87)	65.71–0.0046D (0.16) (nearly constant w/depth)		
Mahanadi Basin	19A	Depth range (mbsf)	0–15	15-100	100–115	115–185	185–300
			72.48–0.335D (0.21)	68.23–0.071D (0.65)	10.06 + 0.537D (0.87) (increases with depth)	85.22–0.123D (0.85)	62.85 + 0.001D (0.02) (nearly constant w/depth)

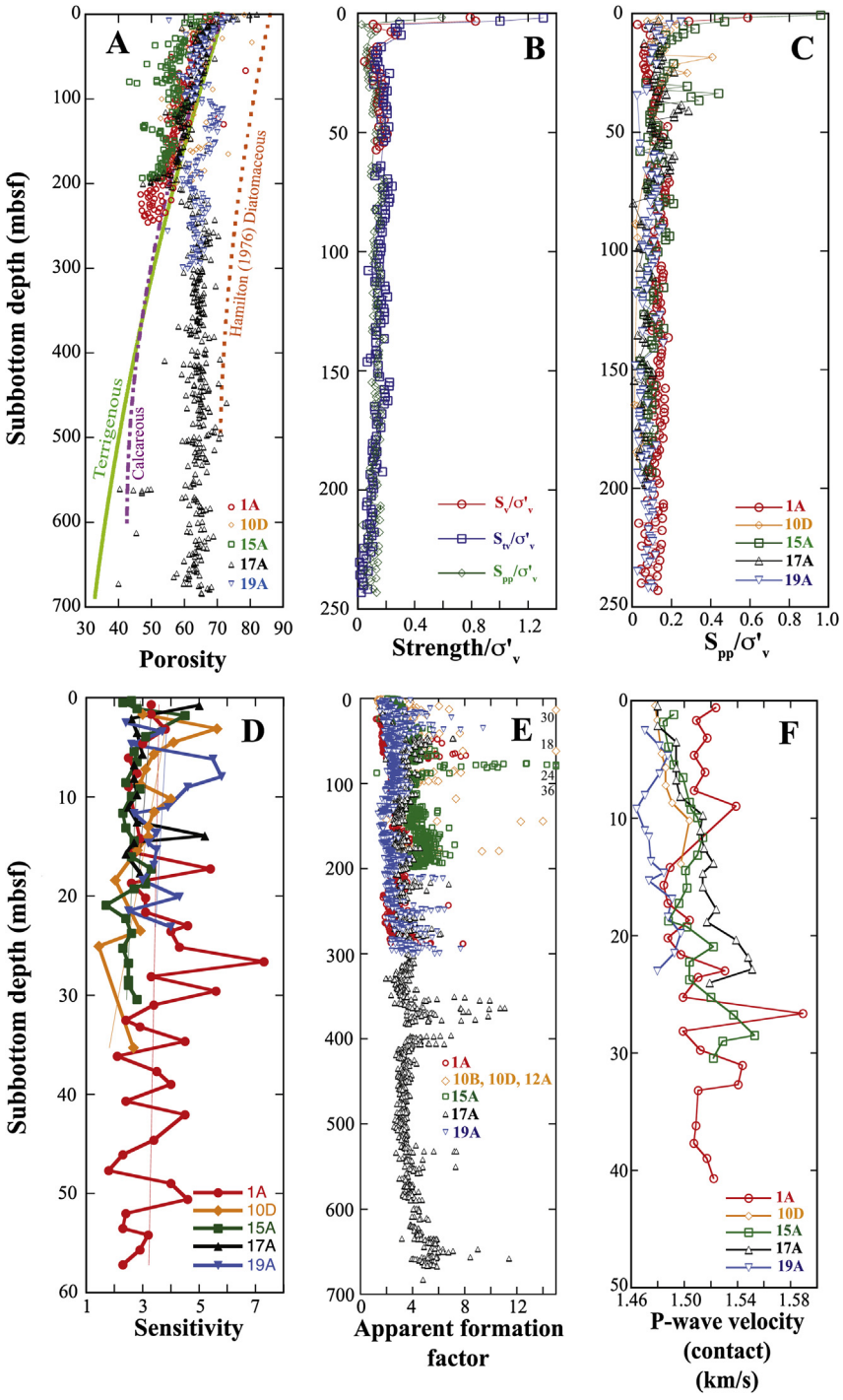

Figure 11. (A). Porosity versus subbottom depth for sediment recovered from five NGHP-01 holes compared to deep-sea sediment trends compiled by Hamilton (1976). Note the near-constant porosity in the lower sections of Holes NGHP-01-17A and −19A. (B). Strength/σ'v versus subbottom depth for Hole NGHP-01-1A. (C). Spp/σ'v versus subbottom depth for five NGHP-01 holes. (D). Mini-vane shear sensitivity versus subbottom depth for five NGHP-01 holes. (E). Apparent formation factor versus subbottom depth for five NGHP-01 holes. (F). Contact P-wave velocity versus subbottom depth for five NGHP-01 holes.

statistically 0.034 Mg/m^3 per 100 m down hole (Table 4), except for four points near the top of the hole (Fig. 7). The specimen with a grain density of 2.33 Mg/m^3 at 86.85 mbsf is from an organic-rich sand recovered in a pressure core.

Along with other properties, the fairly high magnetic susceptibility readings have excursions at about 80 and 133 mbsf, thereby establishing three separate physical property units (Fig. 7). Thermal conductivity values have a median value of 0.94 W/(m*K) and are fairly uniform with depth, decreasing only 0.034 W/(m*K) per 100 m (Tables 3 and 4). Typically, thermal conductivity increases with depth in marine sediment because of greater compaction and pressure (Ratcliffe, 1960). The trend observed here is probably caused by fine-scale gas exsolution.

Sediment subsample, MSCL, and well-log results overall compare favorably except for a small offset in the wireline porosity and bulk density plots between about 131 and 150 mbsf (Fig. 7).

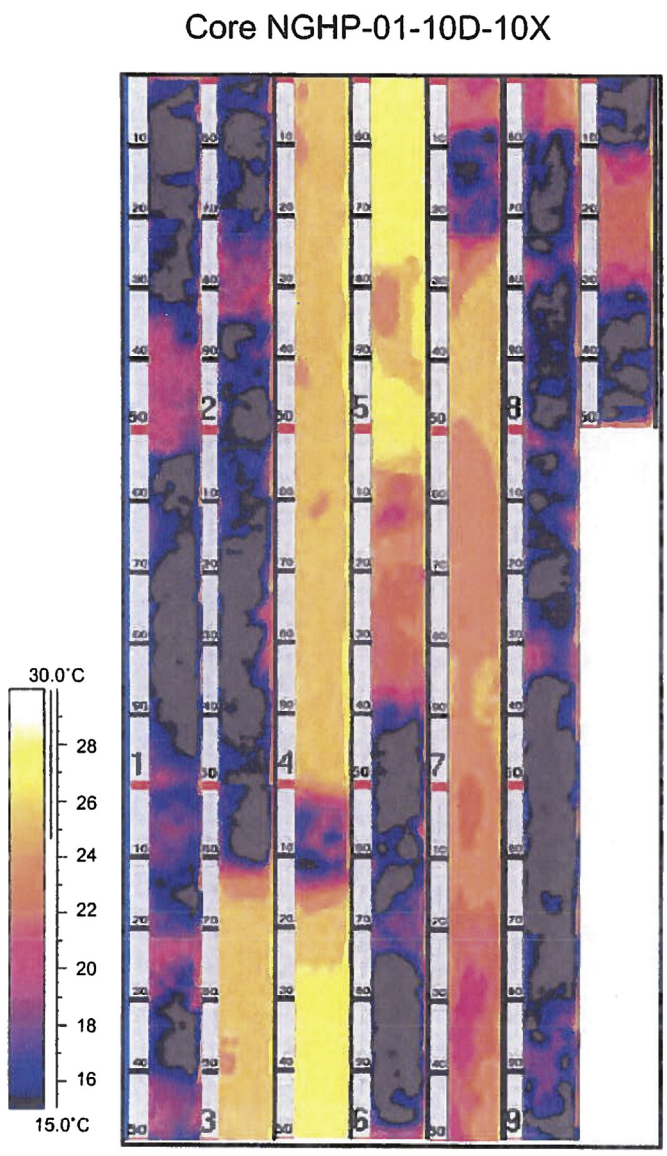

Figure 12. Composite infrared image and temperature scale for Core NGHP-01-10D-10X showing the wide range in temperatures recorded at this depth. Fracture-fill hydrates occupied much of the sediment in this core.

There is only a small increase in the wireline ER in the gas hydrate zone (median: 1.29) versus 1.18 Ωm below the BSR. Median ER values for Wenner and MSCL measurements for the entire hole are 0.78 and 1.13 respectively (Table 3). The Wenner ER values increase while the MSCL decrease by the same amount (0.2 Ωm per 100 m) (Table 4). Both the Wenner and MSCL ER values increase near the sulfate-methane interface (SMI) at about 31.5 mbsf. This increase could be caused by methane coming out of solution below the SMI and disturbing the sediment fabric (Collett et al., 2008a). A small study to determine the effect of intact core "biscuit" sections on Wenner ER measurements revealed no observable trend between 137.85 and 137.94 mbsf (Collett et al., 2008a).

4.1.1.3. Andaman Islands (Hole NGHP-01-17A). Hole NGHP-01-17A, off the Andaman Islands, is composed predominantly of nannofossil oozes that contain little terrigenous material to a subbottom depth of 692 mbsf. The BSR at 608 mbsf, is the deepest of any site drilled as part of the NGHP-01 expedition. The biogenic sediment component consists of various fractions of rapidly deposited calcareous (including foraminifera) and siliceous (including diatoms and spicules) tests (Collett et al., 2008a). The biogenic sediment is interspersed with about 380 pyroclastic layers of varying thickness and color, indicating multiple volcanic events from different sources (Collett et al., 2008a; Rose et al., 2014). Because gas hydrate was not observed in the cores recovered at this site, infrared imaging proved especially valuable in inferring the presence of higher gas hydrate concentrations in numerous ash layers. The IR images had the spatial resolution required to detect individual centimeter-scale ash layers that may not have been discerned by down-hole methods (Collett et al., 2008a) (Fig. 8). Porewater chloride anomalies and other data sets corroborated the IR observations.

Baseline median grain size in Hole NGHP-01-17A, with the coarse material excluded, is 5.1 μm (very fine silt, Wentworth (1929)) (Table 3). The coarser specimens have a median size of 32 μm (Table 3), whereas the ash layer at 464.62 mbsf has a median grain size of 21 μm compared to 4–7 μm for surrounding sediment. Remolded, this ash layer has a different non-plastic/soupy consistency compared to adjacent plastic sediment. The ash (Fig. 13A–B), understandably, has a much smaller biogenic component than surrounding sediment (Fig. 13C–D). Statistically, median grain size increases at a rate of 0.48 μm per 100 m (Table 4) with more scatter lower in the hole (Fig. 8).

At the top of the hole, porosity decreases at a high rate of 109% per 100 m (0–9 mbsf) and then at a lower rate of 6.3% per 100 m (9–200 mbsf) (Table 6, Fig. 8). This rapid decrease from about 82% to 43% at 200 mbsf is overall parallel to Hamilton's (1976) data sets for terrigenous and calcareous deep-sea sediments (Fig. 11A). However, between 200 and 220 mbsf, the porosity increases abruptly to a median of about 64% that is nearly constant (0.46% per 100 m, Table 6) to the bottom of the hole (with an offset at 562 mbsf). Gas hydrate (Fig. 14), which is known to be present in much of this zone under in situ conditions (Collett et al., 2008a), might help stabilize the biogenic structure of the sediment, thereby mitigating the compaction process and causing porosity values to remain relatively stable throughout the zone (Winters et al., 2000b). Clayton et al. (2008), also suggest this mechanism for explaining high porosities in Hole NGHP-01-10B.

An alternate explanation for the porosity change at 200-220 mbsf is the composition of the sediment itself and/or the geologic environment in which it was deposited. The 200–220 mbsf transition in porosity falls near the middle of a lithostratigraphic subunit (Collett et al., 2008a), so any change in composition is subtle. However, there is a continual increase in the biosiliceous content of the coarse fraction beginning at about 220 mbsf from a few percent to about 30% at the bottom of the hole (Collett et al., 2008a). High siliceous biogenic content in marine sediment has been linked to high porosity (e.g., Busch, 1989; Hamilton, 1976; Lee et al., 2013; Taylor, 1991) and even to an increase in gas hydrate saturation (Kraemer et al., 2000). In addition, it has been found to affect the engineering properties of laboratory samples (Tanaka et al., 2003). However, at Hole NGHP-01-17A the explanation is more complicated than just an increase in siliceous microfossils. For one thing, the siliceous content gradually increases below 220 mbsf to a maximum at the bottom of the hole, whereas the effect on porosity is immediate and essentially constant for nearly 500 m of subbottom depth (Fig. 8). The uniformity of porosity with depth is more pronounced in Hole 17A than in other marine sediments, even diatomaceous ooze (Fig. 11A). The high sedimentation rate for sediment in Hole 17A may lead to an underconsolidated state, where the skeletal biogenic framework is not fully supporting the overburden stress. Although, consolidation test results (Section 4.2.4) support this premise, it does not explain why there is not a more pronounced change in the sedimentologic record at 200–220

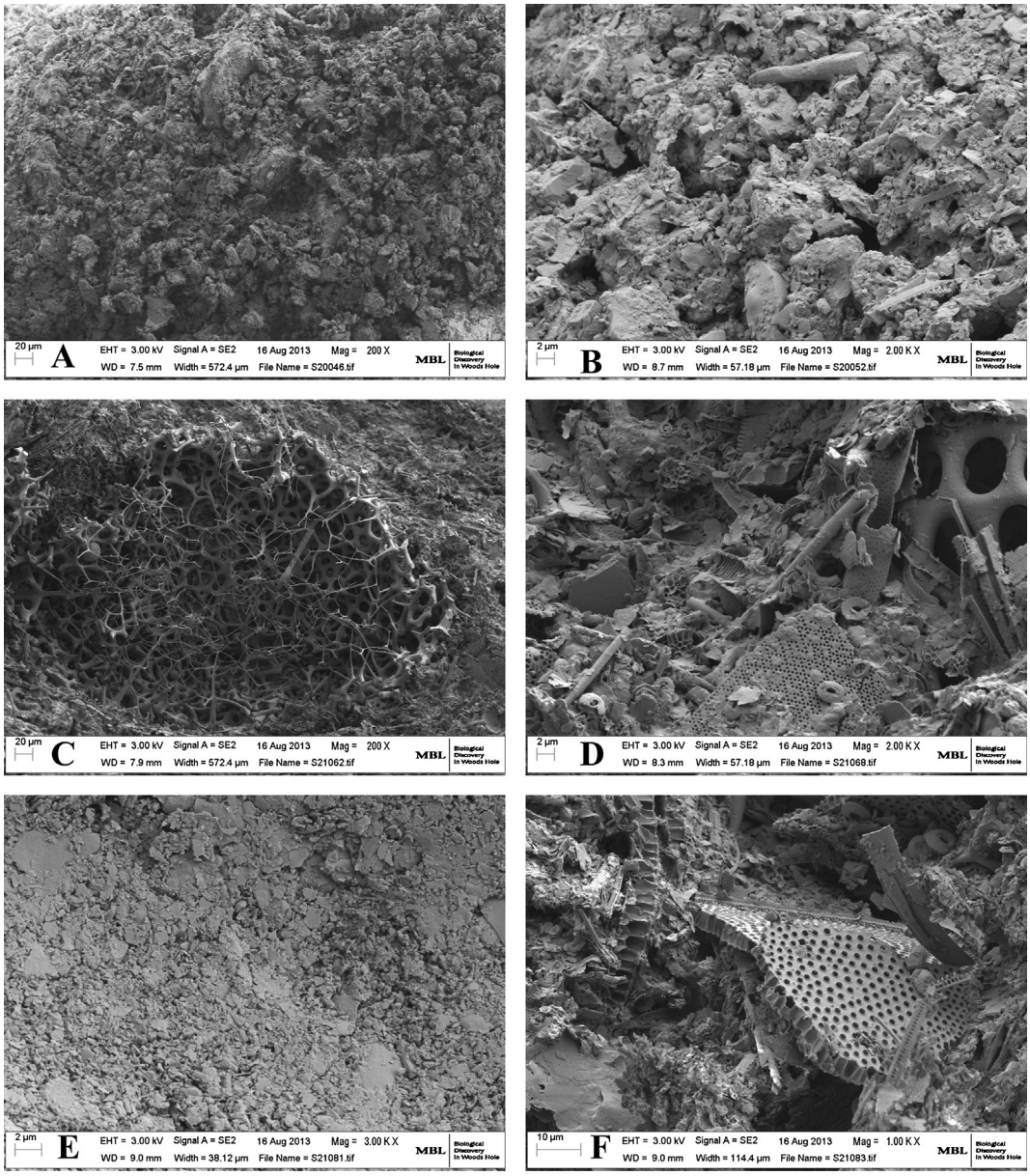

Figure 13. Scanning electron microscope (SEM) images of sediment recovered in Hole NGHP-01-17A: (A–B) Volcanic ash from 464.62 mbsf, (C) Radiolarian (siliceous) from 476.40 mbsf, (D) biogenic sediment from 476.40 mbsf, large items in upper right is a radiolarian (siliceous) and middle bottom is a diatom (siliceous), small donut-shaped tests are coccoliths (calcareous), (E) completely crushed sediment from seating SEM specimen (476.40 mbsf), and (F) sediment immediately adjacent to (E), large pieces are diatoms (siliceous) (photos by L. Kerr, MBL and W. Winters, USGS).

mbsf besides the presence of some authigenic carbonates (Collett et al., 2008a).

The existence of larger, fragile-looking biogenic structures (Fig. 13C) also suggests that the skeletal frame is not fully loaded. The fragility of the biogenic components is demonstrated by their complete destruction by gentle pressure (Fig. 13E), compared to immediately adjacent non-loaded sediment (Fig. 13F). The possible importance of micro-crystalline authigenic carbonate (calcite and magnesite) maintaining high porosity at Site 17 is discussed extensively by Rose et al. (2014). They present compelling evidence of the importance of carbonate precipitates in maintaining anomalously high porosity in these sediments, playing a key role in the localization of gas hydrate.

Grain density values vary from 2.81 to 2.44 Mg/m^3 with a median value of 2.67 Mg/m^3 (Table 3). It decreases statistically at a rate of 0.027 Mg/m^3 per 100 m down hole (Table 4), which coincides with the increase in biosiliceous content.

In Hole 17A, as in all other NGHP-01 drilled holes, different drilling procedures and equipment are used at various subbottom depths to recover the best-quality core in various sediment formations. For example, a hydraulically operated piston corer (APC) is used until the formation becomes too stiff. Then coring continues with a rotary core bit (XCB). This perturbation in porosity and other properties at the APC/XCB boundary is related to the necessity of changing drilling equipment (Fig. 9). Rotary coring often results in the recovery of intact sections of cores (biscuits) surrounded by a disturbed slurry material. A small study in Core NGHP-01-17A-61X found that there was only a 3% difference in water content between intact biscuits and the infilling slurry (Collett et al., 2008a). Thermal conductivity values have a median value of 0.90 W/(m*K) and are

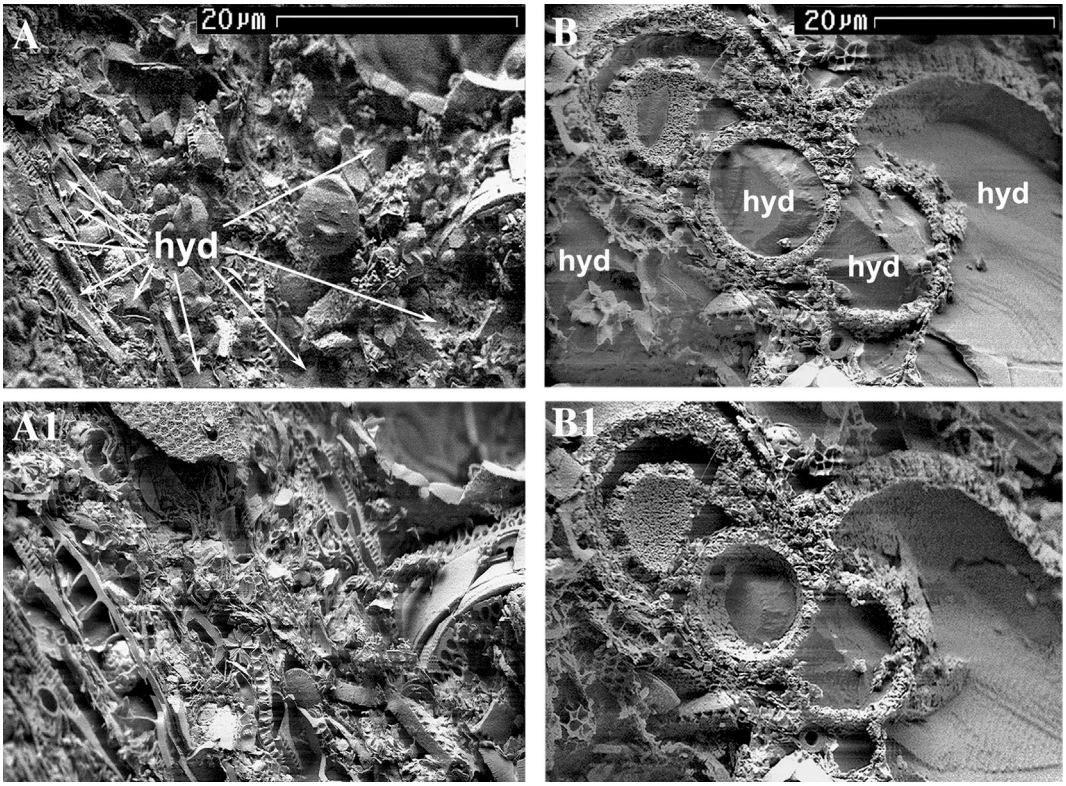

Figure 14. Time lapse scanning electron microscope (SEM) images of sediment from Hole NGHP-01-17A at a depth of 525 mbsf, showing the sublimation of gas hydrate in sediment pores (photos by L. Stern, USGS). Most of the intact shapes are diatoms or Ebridian, both of which are siliceous. Additional SEM images are presented in Stern and Kirby (2008).

fairly uniform with depth, decreasing only 0.033 W/(m*K) per 100 m (Tables 3 and 4). Magnetic susceptibility is low in the hole, reflecting the primary biogenic nature of the sediment (Fig. 8).

Sediment subsample, MSCL, and well-log results compare remarkably well (Fig. 8). Wenner and MSCL median ER values are 0.66 and 0.87 Ωm, respectively, while the wireline median ER values are 0.95 and 0.90 Ωm within and below the BSR (Table 3). A small study was performed on biscuit and infilling material in XCB core NGHP-01-17A-77X. The intact biscuit had an ER of 1.12 Ωm compared to 0.84 Ωm in infilling material, an increase of 33% (Collett et al., 2008a).

4.1.1.4. Mahanadi Basin (Hole NGHP-01-19A). Lithostratigraphically, Hole NGHP-01-19A, in the Mahanadi Basin, contains mainly clay-size grains (70–99%) with a combination of biogenic, authigenic, and volcanogenic material in 15 different lithology types. Sand is rarely encountered. Calcareous nannofossils dominate the biogenic components. Starting at about 180 mbsf, the biosiliceous content begins gradually increasing until it reaches a maximum at the bottom of the hole (Collett et al., 2008a). Infrared images and interstitial water analyses imply that gas hydrate is disseminated as pore- or fracture-filling within the clay-size fraction. Median hydrate saturation from well-log records is about 3% (Table 3).

Baseline median grain size in Hole NGHP-01-19A is 4.8 μm (very fine silt size, Wentworth (1929)) (Table 3). Statistically, median grain size increases at a rate of 0.19 μm per 100 m (Table 4) with more scatter higher in the hole (Fig. 9).

Supporting the lithostratigraphic assessment that Hole NGHP-01-19A is the most complex of NGHP-01, five straight-line segments were required to describe porosity versus depth in the hole (Tables 5 and 6). Porosity decreases from 73% at a high rate in the top of the hole, actually increases with depth from 100 to 115 mbsf, and changes little with depth (0.1% per 100 m) below about 185 mbsf (Table 6) to reach 61% at the bottom of the hole. The porosity versus depth relation is adjacent to Hamilton's (1976) data sets for terrigenous and calcareous deep-sea sediments to 100 mbsf, but then diverges below that depth (Fig. 11A). Interestingly, at the depth when porosity versus depth becomes constant (~185 mbsf), there is, once again, a continual increase in the biosiliceous content of the coarse fraction to the bottom of the hole (Collett et al., 2008a). An ash layer at 7.51 mbsf has a porosity of 55%.

Grain density values vary from 2.76 to 2.62 Mg/m^3 with a median value of 2.70 Mg/m^3 (Table 3) except for the ash layer at 7.51 mbsf with a grain density of 2.40 Mg/m^3. Although grain density varies considerably down hole, there may be a slight decrease with depth below 185 mbsf.

Thermal conductivity values have a median value of 0.92 W/(m*K) and are fairly uniform with depth, decreasing only 0.021 W/(m*K) per 100 m (Tables 3 and 4). Although significant variation exists above about 60 mbsf, magnetic susceptibility overall is low in the hole, reflecting the primary biogenic nature of the sediment (Fig. 9).

Except for a slight offset between the MSCL and core ER data, sediment subsample, MSCL, and well-log results compare remarkably well (Fig. 9). Wenner and MSCL median ER values are 0.49 and 0.94 Ωm, respectively, while the wireline median ER values are 0.86 and 0.81 Ωm within and below the BSR (Table 3).

4.1.2. Comparison of NGHP-01 regions

Gas hydrate saturation varies from non-existent (Hole NGHP-01-1A) to high (Hole NGHP-01-10D), with intermediate hydrate saturations in other holes. Note that post-cruise analysis, that accounts for the complex nature of hydrate veins at Site NGHP-01-

10D, has reduced some hydrate saturation values (Cook et al., 2010). The character of the hydrate at this site also varies considerably from disseminated, pore-filling, and nodular, to highly complex high-angle thin veins (Table 7) (Collett et al., 2008a; Collett et al., 2014; Collett et al., 2008b). Sediment characteristics and behavior have similarities and major differences between different NGHP-01 regions and even within the same basin.

Fine-grained sediment cores recovered from other sites during the NGHP-01 expedition contained grain-displacing hydrate with different habits, including nodules, laminar veins, fracture fill, and highly complicated, multi-rotational, thin high-angle lenses (for example, Fig. 3a) (Collett et al., 2008a; Holland et al., 2008; Priest et al., 2008). The formation of these extremely complex rotational hydrate features that appear to be "twisted" and induced by core rotation during the drilling process, actually may reflect natural conditions because some recovered cores with these rotational hydrates were obtained as push cores, unaffected by drill-bit rotation (M. Holland, personal communication, 2008). However, sampling effects, including effective stress reduction, fracture formation, and hydrate reformation, may be responsible for some coring-related artifacts (Yun et al., 2010). Hydraulic fracturing caused by the advection of pore fluids may have caused some hydrate to form at Site NGHP-01-10 in the KG Basin (Rees et al., 2011). The chaotic nature of the fractures at Site NGHP-01-10 also imply high gas flux (Cook and Goldberg, 2008b), unlike at Site NGHP-01-5 in the KG Basin where fractures are thought to be limited to less than a few meters in length (Cook and Goldberg, 2008a). Calculation of gas-hydrate pore saturation in these complex hydrate morphologies is challenging and may require additional analysis techniques (e.g., Ghosh et al., 2010; Lee and Collett, 2009b), because traditional techniques may overestimate hydrate saturations (Shankar and Riedel, 2011). Hydrate habit has an important effect on understanding formation mechanisms, accurate modeling and prediction, gas recovery during dissociation, and sediment response and properties. Not only do sediment characteristics affect hydrate habit, but hydrate growth also affects numerous properties and the behavior of the host material, perhaps including sediment dewatering (Clennell et al., 1999; Judd and Hovland, 2007; Riedel et al., 2010).

4.1.2.1. Grain size. The composite statistics, organized by the overall NGHP-01 project and region, indicate that drilled locations around India are predominantly fine grained (very fine silt) (Table 2). Median (D_{50}) and mean grain sizes (MGS) for individual regions vary from 4 μm in the KK Basin to twice as large (7–8 μm) in the KG Basin, where coarser sediments occur (Fig. 7). Regional ternary grain-size plots also indicate that sediments are predominantly clayey silt to silty clay in size (Fig. 10). Average regional tendencies are towards a fine skewness (positive skewness parameter) and broader peak than a normal distribution (negative

Table 7
Gas hydrate, reservoir, grain-size, porosity, and Atterberg limit characteristics for various field projects. Mean properties are reported for particular sites or drilled subbottom intervals. Project-wide grain-size analyses were not performed for ODP Leg 164, ODP Leg 204, and IODP X311 as part of this study.

Project	Area	Site/ Layer	GH character	General reservoir character	Reservoir sediment description	GH pore saturation (max) (%)	D_{50} (μm)	Grain size (max//min) (μm)	Grain size sand//silt//clay (median) (%) (max) (%) (min) (%)	Porosity (median) (%)	Porosity (max//min) (%)	LL//PL
Marine												
NGHP-01	India											
	KG Basin	10	Veins, nodules, disseminated	Fine grained	Nannofossil-bearing clay	85	6	14//3		63	81//51	98–70/ /49-33
	KG Basin	15	Pore filling	Coarser grained		40	19	169//4				
	Andaman Is	17	Pore filling	Ash beds and ash-rich zones within a finer matrix	Nannofossil ooze	>50	6	55//2		64	82//4	96-81/ /59-32
	Central Mahanadi Basin	19	Diffused	Fine grained	Clay with volcanic glass, pyrite, carbonate, aragonite, organics, nannofossils, foraminifera	~15	5	57//4		64	75//55	110-91/ /70-34
JIP Leg 1	N. GoM	AT13-2	–		Fine grained	~10–20	2	2//1		60	65//48	
		KC151-3	Fractures+		Fine grained	>20	2	7//1		50	73//44	
Marion Dufresne (MD02)	N. GoM	–	Discrete massive layers		Fine grained	100			0.2//22//77 7//40//95 0.0//5//54	66	96/56	
Arctic												
Mount Elbert	AK N Slope	D-GH	Pore filling	Coarse grained	Very fine sand	76	65	107//10		47-33	47-42	
		C-GH1	Pore filling	Coarse grained	Coarse silt	77	60	97//41		45–36	45–39	
		C-GH2	Pore filling	Coarse grained	Fine sand	65	190	210//162		43–26	43–26	
Mallik	NWT, Canada	2L	Pore filling	Coarse grained	Sand, gravel							
		5L	Pore filling	Coarse grained	Sand, gravel	89	104–141 (mean)	337//11		35 (mean)	44//24	

GoM: Gulf of Mexico; KG: Krishna-Godavari; LL: Liquid Limit; PL: Plastic Limit; D_{50}: Median grain size; Note: Coarse-vs fine-grained are general terms and do not describe exact grain size.

kurtosis, except for the KK Basin) (Table 2). Except for coarser layers in NGHP-01-15A, the median of fine-grained matrix sediment typically changes little with depth at an average rate of 0.22 μm per 100 m. Hole NGHP-01-17A changes at the highest rate of 0.48 μm per 100 m (Table 4).

Separate grain-size analyses were also performed on 23 Indian sediment samples from Sites NGHP-01-10, -14, -15, -17, and -19 that were associated with infrared cold spots (Collett et al., 2008a; Long et al., 2009; Torres et al., 2008) indicative of gas hydrate dissociation (Torres et al., 2008). Mean and median grain-size values for the IR samples were larger than respective parameters for each region (Table 2). In addition, a coarser-grained 5–8 m thick layer at Site 15 (Figs. 7 and 10), contained 20–40% pore-filling hydrate (Riedel et al., 2011). Compiled NGHP-01 site data (Table 7) does indeed corroborate the presence of larger grain-sizes at Site 15.

4.1.2.2. Index properties. With a few exceptions in Holes NGHP-01-15A and -17A, porosity typically decreases with subbottom depth in all NGHP-01 holes. This occurs rapidly near the seafloor at rates up to about 190% per 100 m to small rates of only 0.1% per 100 m (Table 6). Because median grain size typically is fairly uniform with depth, or only changes gradually (Section 4.1.2.1), other reasons explain the wide range in compaction behavior. Considering that no universal compaction curve exists for even similar types of sediment (Hamilton, 1976) because of the complexities in textural, compositional, chemical, porewater, depositional environment, stress history, age, and other attributes of a particular reservoir, there is fairly close agreement to Hamilton's (1976) terrigenous and calcareous porosity versus depth relationships in the upper section of the holes (Fig. 11A). However, NGHP-01-15A and -17A have little change in porosity in the lower section of each hole. Hole NGHP-01-17A has fairly constant porosity for nearly 500 m. The constant porosity is probably related to an increase in siliceous biogenic content coupled with high sedimentation rates to create an underconsolidated (Section 4.2.4) framework in which full effective stresses are not transferred to the grain structure of the sediment, which can be destroyed by compressional forces (Fig. 13E). The subbottom depth at which each process dominates is related to a complex set of criteria. Porosity trends suggest that gravitational forces become dominant by approximately 3–24 mbsf (Table 6), whereas normalized NGHP-01 strength measurements imply the depth is closer to 10-14 mbsf (Table 4).

In most regions occupied during NGHP-01, grain density typically is within the range of 2.6–2.8 Mg/m^3 (Table 4). Isolated exceptions do occur as well as in the bottom of Hole NGHP-01-17A. A pronounced grain density decrease in NGHP-01-17A is probably inversely related to biosilica content.

Although, magnetic susceptibility varies considerably down- and between holes, it is directly related to primary and secondary magnetic mineral or biogenic content of the sediment. It is less than 20×10^{-5} SI for major portions of Hole NGHP-01-17A (Fig. 8) to 500×10^{-5} SI in other holes.

Measurements performed on longitudinally split core sections, MSCL results from whole cores, and down-hole well-log interpretations typically are supportive. In most instances when the data diverge, it is because of an explainable natural event. For example, the presence of in situ gas hydrate in Hole NGHP-01-10D (Fig. 6) increases ER significantly compared to measurements performed on cores after hydrate dissociated.

Thermal conductivity varied down hole, possibly as the result of gas expansion deeper in the hole, causing measured values to be less than those measured across northern Cascadia (Davis et al., 1990) and occasionally even below that of seawater (~0.56–0.58) (Kim and Yun, 2013).

Below an upper 10–14 m deep zone that exhibits pseudo-overconsolidated behavior, undrained pocket penetrometer shear strength divided by the vertical effective stress (S_{pp}/σ'_v) slowly decreases with depth, typically remaining below 0.22 (Table 4, Fig. 11C). Strength/σ'_v values approximate 0.22 in the upper part of all holes, but increasingly diverge from 0.22 with depth as a result of coring disturbance (below the APC/XCB boundary) or pocket penetrometer limitations (220–250 kPa, Section 3.7) (Figs. 5–9). The implication is that these sediments have not been heavily overconsolidated due to geologic mass wasting or other events.

Vane shear strength sensitivity (peak/remolded strength) varies from about 1 (insensitive) to 7 (medium sensitive or sensitive; Holtz and Kovacs, 1981; Hunt, 1984) in all holes (Fig. 11D) with median values between 2.6 and 3.5 (Table 3). Values are much lower than "quick" clays which can reach sensitivities of more than 500 (Lambe and Whitman, 1969). Quick conditions can be caused by uplifting and leaching marine clays or the break down of volcanic ash (Terzaghi and Peck, 1967). Any process that disturbs or remolds NGHP-01 sediment must account for subsequent strength loss that typically will result.

The apparent formation factor, which relates resistivity of saturated sediment to that of the pore fluid, provides insights into the interrelationships between the solid and void spaces in the sediment and can be used to interpret relative flow through porous media. Normalizing the Wenner resistivity measurements to those of seawater produced values between 2 and 36 for all holes (Fig. 11E). Median values for each hole varied from 2.45 to 3.88 (Table 3). Typically, apparent formation factor values increase with depth (Table 4, Fig. 11E). These values are close to or within the range of 1.57–3.70 reported by Boyce (1968). Spikes in apparent formation factor may be caused by the presence of coarser-grained layers.

Median contact P-wave velocities are similar, varying from 1.48 to 1.51 km/s (Table 3), and generally increasing with depth (Table 4, Fig. 11F). These values are close to that of seawater (Yun et al., 2010) reflecting the high porosity of the sediment. Measurements typically could not be completed below the SMI because of the presence of gas in the sediment. However, in Hole NGHP-01-1A, because of the lack of interstitial gas, results followed a linear trend to below 40 mbsf (Fig. 11F) (Collett et al., 2008a).

4.2. Marine and permafrost-related gas hydrate comparisons

Although the properties of host sediment, to a large extent, influence hydrate characteristics, a complex system of factors combine with a particular timing to control particular gas hydrate habits. If any one of the factors is missing or timing is modified then hydrates may not form at all, or may take a different form. However, gas hydrate typically forms as either (a) sediment pore-filling hydrate consisting of very small individual grains (e.g., Fig. 3E) or (b) sediment grain-displacing clean fracture-filling, layered, or complex veined hydrates in fine-grained marine sediment (e.g., off India and in the northern Gulf of Mexico) (Table 7, Figs. 3A–D) (Collett et al., 2008a; Cook and Goldberg, 2008a, b; Winters et al., 2007a).

4.2.1. Grain size

At the Mount Elbert well on the Alaskan North Slope and the Mallik wells on the Mackenzie Delta, NWT (Fig. 1), >10-m thick gas hydrate-bearing (GHB) sandy deposits are capped by finer-grained sediments that may reduce gas migration (Dallimore and Collett, 2005; Dallimore et al., 1999b; Hunter et al., 2011; Winters et al., 2011; Winters et al., 1999a; Winters et al., 2005).

Several key observations related to hydrate bearing units D-GH, C-GH1, and C-GH2 at the Mount Elbert well provide insight into the geologic factors controlling hydrate formation in an Arctic

permafrost-related setting (Fig. 15) (Winters et al., 2011). Units D-GH, C-GH1, and C-GH2 (Fig. 15) have: (1) maximum sand contents of 81%, 74%, 95% and (2) high average sand contents of 51%, 48%, and 90%. The seal layers contain only 1%, 18%, and 28% sand, but have an average of 29%, 20%, and 13% clay-size particles (an increase of 2.9, 2.1, and 7.3 times the amount of clay in the coarser underlying hydrate-bearing sediment) (Winters et al., 2011).

These data indicate that the greatest concentrations of gas hydrate are typically present in coarser-grained deposits that are bounded by finer-grained sediment. Average mean grain size (MGS) of GHB sediment from the Mallik 2L well is ~111 μm, compared to overlying sediment with an average MGS of ~32 μm (Winters et al., 2000a). Inter-bedded finer-grained sediment, however, may also contain some gas hydrate. Sandy GH reservoirs are not only present in permafrost-related Arctic locations, but are also offshore, e.g., Nankai Trough (Uchida and Takashi, 2004)) and the Gulf of Mexico (Hutchinson et al., 2008a; Robertson et al., 2013; Boswell et al., 2012).

If conditions are conducive to forming large fracture-filled reservoirs, such as in Hole NGHP-01-10D (Figs. 3B, 4), then large quantities of gas hydrate may form in a fine-grained environment. Although the processes responsible for forming fracture-filling reservoirs is still being studied, hydraulic fracturing and high gas flux may be involved (Cook and Goldberg, 2008b; Cook et al., 2010; Rees et al., 2011).

4.2.2. Index properties

Bulk index properties, including water content, often correlate to sediment behavior (Bryant and Trabant, 1972; Keller, 1974) and reflect the degree of compaction and stress history at various subbottom depths. Grain-size measurements that classify the NGHP-01 and IODP X311 sediment as silty clay or clayey silt are in agreement with index properties, including the Atterberg limits classification of highly plastic clay or compressible silt (Table 8). The consistent fine-grained character of the sediment is reflected in the very high dry strength possessed by nearly all tested specimens. However, other index properties do change with subbottom depth. This variability is also reflected in the pocket penetrometer strength values, which range from <12 kPa to above 240 kPa. This variation could result from sample disturbance, especially when strength values are low at significant subbottom depths (Table 8).

Water contents of the index property whole-round samples from NGHP-01, IODP X311, and ODP Leg 164 vary from 88 to 24% and are related to subbottom depth in some holes (IODP X311 U1327C) and not others (Table 8). Typically a decrease in water content with depth is the result of normal compaction. However, significant variability does occur down hole, and occasionally water content does not decrease with depth (for example, NGHP-01 Hole 17A) possibly reflecting high nannofossil ooze content (Collett et al., 2008a). Liquid limits range from 110 to 56, and plastic limits from 70 to 23 (Table 8). All LI values are less than 1.0, reflecting the influence of subbottom depth.

NGHP-01 regional median porosity (volume voids/total volume) values are essentially identical (63–64%) between the KG Basin, offshore the Andaman Islands, and the Mahanadi Basin, in agreement with the similarity in their median grain sizes (Table 7). Although median porosity values (26–47%) for samples obtained in permafrost-related gas hydrate reservoirs are considerably lower than for marine sediments, the actual size of the pores are larger, thereby promoting the formation of gas hydrate (Winters et al., 1999a). Previous studies have shown that for similar sediment types and test conditions, higher porosity specimens generate more

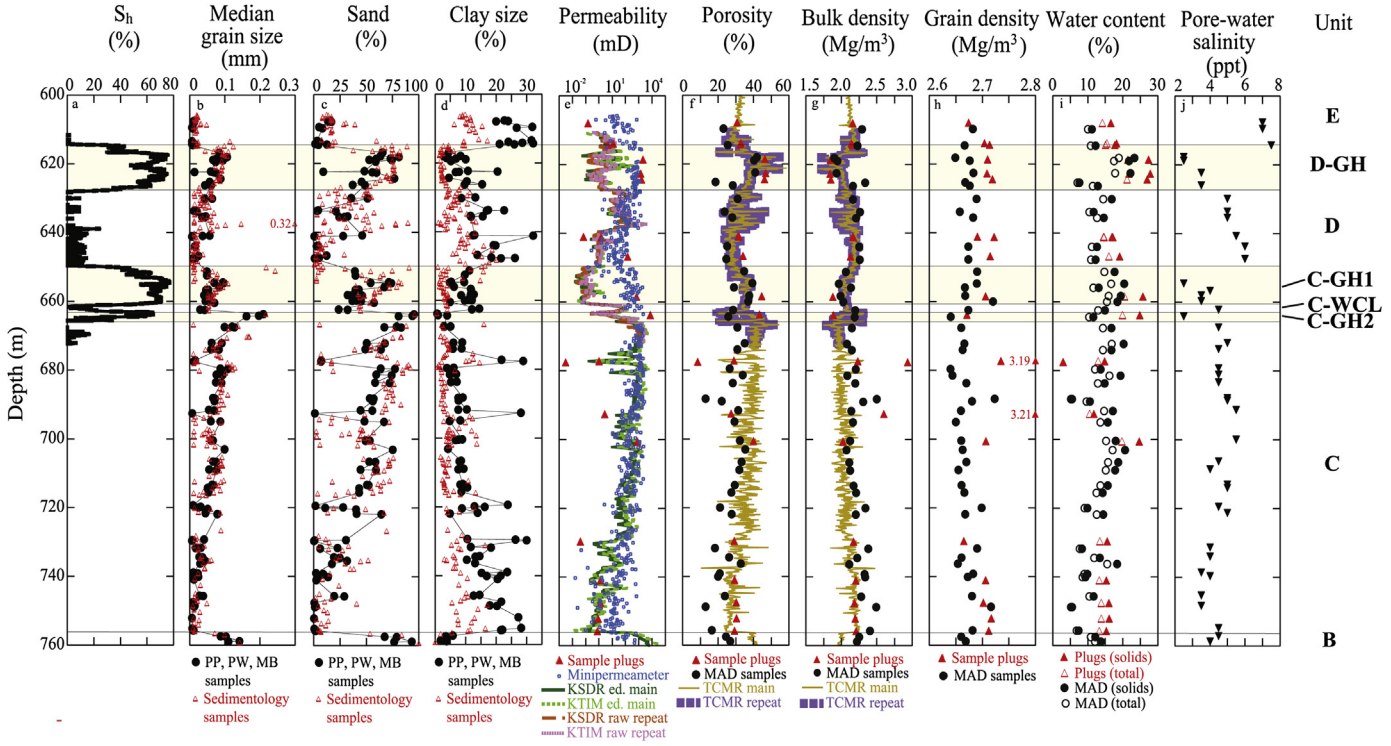

Figure 15. Profiles of sediment properties from the Mount Elbert well including: (a) gas hydrate pore saturation (Sh) determined using the NMR-DEN POR method from the TCMR-repeat-pass-plus-density log (Lee and Collett, 2011), (b, c, and d) median grain size, percent sand, and percent clay-size determined from laser-grain-size analyses on physical property (PP), pore water (PW), microbiology (MB), and sedimentology (Rose et al., 2011) samples, (e) permeability measurements from core plugs, slabbed core using a mini-permeameter, and well logs, (f) porosity values determined from sample plugs, moisture and density (MAD) subsamples, and TCMR log runs, (g) bulk density determined from sample plugs, moisture and density (MAD) subsamples, and TCMR log runs, (h) grain density determined from sample plugs and moisture and density (MAD) subsamples, (i) water content (based on mass of solids and total sample mass), and (j) pore water salinity (Torres et al., 2011) (Winters et al., 2011).

Table 8
Index properties for the NGHP-01, IODP X311, and ODP Leg 164 projects.

Project	Boring ID	Depth (m)	wc (%)	LL	PL	PI	LI	S_{PP} (ave) (kPa)	S_v (kPa)	S_t	Dry strength	Dilentancy	Toughness	Unified classification
NGHP-01	10D	18.80	60	82	49	33	0.33	40			Very high	Slow	Low	MH/OH
NGHP-01	10D	38.76	74	98	36	62	0.61	12			Very high	None	Low	CH/OH
NGHP-01	10D	64.02	71	82	33	49	0.78	<12			Very high	Slow	Low	CH/OH
NGHP-01	10D	93.27	52	82	35	47	0.36	65			Very high	Slow	Low	CH/OH
NGHP-01	10D	103.7	49	70	39	31	0.32	<12			Very high	Slow	Low	MH/OH
NGHP-01	10D	111.50	64	84	33	51	0.61	<12			Very high	Slow	Low	CH/OH
NGHP-01	17A	38.80	62	84	32	52	0.58	55			Very high	None	Medium	CH/OH
NGHP-01	17A	131.00	56	81	42	39	0.36	55			Very high	Slow	Low	MH/OH
NGHP-01	17A	177.80	54	88	44	44	0.23	45			Very high	Slow	Low	MH/OH
NGHP-01	17A	253.80	62	85	51	34	0.32	40			Very high	Slow	Low	MH/OH
NGHP-01	17A	332.80	65	85	59	26	0.23	90			High	Slow	Low	MH/OH
NGHP-01	17A	420.30	69	96	57	39	0.31	250			Very high	Slow	Low	MH/OH
NGHP-01	18A	53.32	60	97	46	51	0.27	60			Very high	Slow	Low	MH/OH
NGHP-01	19A	28.60	72	91	46	45	0.58	12			Very high	Slow	Low	MH/OH
NGHP-01	19A	81.50	64	110	65	45	−0.02	70			Very high	Slow	Low	MH/OH
NGHP-01	19A	120.20	83	105	70	35	0.37	25			Very high	Slow	Low	MH/OH
NGHP-01	19A	168.80	71	108	34	74	0.50	30			Very high	Slow	Low	CH/OH
NGHP-01	19A	207.70	67	101	55	46	0.26	25			Very high	Slow	Low	MH/OH
NGHP-01	19A	265.80	66	91	53	38	0.34	90			Very high	Slow	Low	MH/OH
IODP X311	U1327C	19.85	53	63	23	40	0.75	40			Very high	Slow	Low	CH/OH
IODP X311	U1327C	50.35	34					60						
IODP X311	U1327C	88.55	32	56	30	26	0.08	>240			Very high	Slow	Low	CH/MH/OH
IODP X311	U1327C	185.02	24					>240						
IODP X311	U1327C	210.60	29	65	26	39	0.08	>240			Very high	Slow	Low	CH/OH
IODP X311	U1329C	21.85	51	62	25	37	0.70	30			Very high	Slow	Low	CH/OH
IODP X311	U1329C	32.85	47	61	32	29	0.52	90			Very high	Slow	Low	MH/OH
IODP X311	U1329C	131.9	38	66	28	38	0.26	205			Very high	Slow	Low	CH/OH
IODP X311	U1329C	146.2	47	74	39	35	0.23	<12			Very high	Slow	Low	MH/OH
IODP X311	U1329C	165.1	47	91	55	36	−0.22	<12			Very high	Slow	Low	MH/OH
ODP Leg 164	995A	3.09	63	68	24	44	0.89	22	25	6.2				
ODP Leg 164	995A	49.57	88					55	55	4.2				
ODP Leg 164	995A	148.48	60	99	35	64	0.39	120	135	4				
ODP Leg 164	995A	253.40	52					94	130	6.8				
ODP Leg 164	995A	350.80	44	83	35	48	0.19	>230						
ODP Leg 164	995A	467.00	38											
ODP Leg 164	995A	546.11	52	82	40	42	0.29							
ODP Leg 164	995A	666.85	39											

wc: Water content; LL: Liquid Limit; PL: Plastic Limit; LI: Liquidity Index; S_{pp}: Pocket penetrometer strength; S_v: Vane shear strength; St: Sensitivity; CH: Clay, high plasticity; MH: Silt, high compressibility; OH: Organics, high compressibility.

positive pore pressure during shear, are weaker, and can have lower acoustic velocities than samples with lower porosity (Atkinson, 1993; Carmichael, 1982).

4.2.3. *Effect of grain size and index properties on permeability*

It is apparent that grain size affects a number of other properties such as porosity and permeability. At the Mount Elbert well, intrinsic permeability differences between hydrate-bearing sediments and respective seals were measured (Winters et al., 2011). The average plug permeabilities to air of Unit D-GH and the seal above it are 1700 mD and 5.7 mD; the average plug permeabilities of Unit C-GH1 and the seal above it are 675 mD and 49 mD (Fig. 15) (Winters et al., 2011). The seals are 300 and 14 times less permeable than the underlying sediment. A correlation between median grain size and measured permeability of plugged core is responsible for much of the difference (Winters et al., 2011). An extensive set of mini-permeameter tests reasonably compare with well-log results outside of hydrate-bearing zones (Fig. 15). Differences between intrinsic values measured by the mini-permeameter and in situ values estimated from the Schlumberger-Doll Research permeability (KSDR) repeat log are mainly the result of gas hydrate presence. Average intrinsic permeabilities for the D-GH, C-GH1, and C-GH2 hydrate layers are 550 mD, 300 mD, and 2150 mD, respectively. In situ permeabilities for the same layers are 1.8 mD, 0.1 mD, and 54 mD; factors that are 300, 3000, and 40 times less than intrinsic values (Winters et al., 2011). One of the most important relationships influencing the occurrence of in situ gas hydrate is between permeability and porosity. At the Mount Elbert well, for specimens with porosity values between 25 and 45%, a change of 4 percentage points in porosity changes permeability by an order of magnitude (Winters et al., 2011). Not only is adequate permeability important for hydrate formation in reservoirs, it is also critical to ensure adequate transport of gas during the hydrate formation stage, and during production of gas from controlled dissociation.

4.2.4. *Consolidation*

Constant-rate-of-strain consolidation tests were performed to evaluate the stress history and confined deformation properties of NGHP-01, IODP X311, and ODP Leg 164 sediment (Table 9, Fig. 16). The consolidation results vary widely. The maximum past stress determined from shallow subbottom sediment samples was occasionally larger than the in situ vertical effective stress, indicating the sediment was pseudo-overconsolidated (OCR>1) nearer the seafloor (Table 9, Fig. 16). This may be related to inter-particle electrical properties in shallow fine-grained sediment (Francisca et al., 2005) and is not an indication that the specimen behaves as stiff, heavily overconsolidated sediment. However, the maximum past stress was significantly less than the in situ vertical effective stress in many of the samples. This is indicated by negative σ'_e values and OCRs less than 1.0. The NGHP-01 and ODP Leg 164 samples exhibit a trend of decreasing OCR with depth (Fig. 16). Compression indices (C_c) varied from 0.13 to 1.38, however the

Table 9
Consolidation properties for the NGHP-01, IODP X311, and ODP Leg 164 projects.

Project	Boring ID	Depth (m)	wc (initial) (%)	e_o	e_f	σ'_{vo} (kPa)	σ'_{vm} (kPa)	σ'_e (kPa)	OCR	C_c	C_r	c_v (in situ) (m^2/s)	c_v (max) (m^2/s)	c_v (virgin) (m^2/s)
NGHP-01	10D	18.8	58.9	1.62	0.75	89.8	77	−12.8	0.86	0.54	0.11	4.0×10^{-8}	5.0×10^{-8}	3.0×10^{-8}
NGHP-01	10D	38.76	95.9	2.65	1.17	195.7	54	−141.7	0.28	0.80	0.16	2.8×10^{-8}	3.5×10^{-8}	1.5×10^{-8}
NGHP-01	10D	64.02	58.9	1.67	0.73	341.5	41	−300.5	0.12	0.49	0.14	2.2×10^{-8}	3.0×10^{-8}	2.0×10^{-8}
NGHP-01	10D	93.27	72.1	2.12	0.98	544.3	52	−492.3	0.10	0.65	0.17	1.5×10^{-8}	5.5×10^{-8}	3.5×10^{-8}
NGHP-01	10D	111.5	49.0	1.59	0.49	664	130	−534	0.20	0.62	–	1.0×10^{-8}	1.5×10^{-7}	1.0×10^{-8}
NGHP-01	17A	38.8	62.9	1.79	1.07	204	390	186	1.91	0.69	0.08	3.0×10^{-7}	3.0×10^{-7}	3.0×10^{-7}
NGHP-01	17A	131	53.7	1.57	0.9	778	370	−408	0.48	0.68	0.12	1.0×10^{-7}	7.0×10^{-8}	3.5×10^{-8}
NGHP-01	17A	177.8	63.4	1.75	1.09	1091	150	−941	0.14	0.56	0.14	3.5×10^{-8}	9.0×10^{-8}	5.0×10^{-8}
NGHP-01	17A	253.8	60.4	1.83	1.19	1583	480 (?)	−1103	0.30	0.69	0.12	1.0×10^{-7}	2.1×10^{-7}	1.5×10^{-7}
NGHP-01	17A	332.8	63.3	1.94	1.31	2029	370	−1659	0.18	0.65	0.11	3.5×10^{-7}	6.0×10^{-7}	3.5×10^{-7}
NGHP-01	17A	420.3	73.2	2.24	1.63	2530	130 (?)	−2400	0.05	0.40	0.07	8.0×10^{-7}	1.9×10^{-5}	8.0×10^{-7}
NGHP-01	18A	53.32	55.5	1.69	0.98	288	330	42	1.15	0.71	0.12	6.0×10^{-8}	2.0×10^{-7}	3.0×10^{-8}
NGHP-01	19A	28.6	76.4	2.11	0.96	135	150	15	1.11	0.77	0.14	4.0×10^{-8}	4.0×10^{-8}	2.0×10^{-8}
NGHP-01	19A	81.5	64.8	1.83	1	455	420	−35	0.92	1.02	0.15	2.2×10^{-7}	2.2×10^{-7}	5.0×10^{-8}
NGHP-01	19A	120.2	83.7	2.6	1.18	679	340	−339	0.50	1.32	0.18	1.8×10^{-7}	3.0×10^{-7}	5.0×10^{-8}
NGHP-01	19A	168.8	69.9	2.05	1.11	925	370	−555	0.40	1.00	0.15	1.8×10^{-7}	2.0×10^{-7}	5.0×10^{-8}
NGHP-01	19A	207.7	60.4	1.86	1.08	1171	580	−591	0.50	0.98	0.15	1.0×10^{-7}	1.4×10^{-7}	5.0×10^{-8}
NGHP-01	19A	265.8	64.7	1.89	1.26	1510	800	−710	0.53	0.94	0.10	1.0×10^{-7}	2.0×10^{-7}	8.0×10^{-8}
IODP X311	U1327C	19.85	48.0	1.41	0.73	130	120	−10	0.92	0.43	0.02	2.6×10^{-7}	2.6×10^{-7}	2.6×10^{-7}
IODP X311	U1327C	50.35	34.0	1.16	0.66	363	215	−148	0.59	0.39	0.06	6.0×10^{-8}	6.0×10^{-8}	6.0×10^{-8}
IODP X311	U1327C	88.55	33.0	1.06	0.88	662	1310 (?)	648	1.98	0.35	0.06	7.0×10^{-7}	6.0×10^{-7}	5.0×10^{-7}
IODP X311	U1327C	185.02	24.0	0.82	0.65	1454	225	−1229	0.15	0.13 (?)	0.02	4.0×10^{-4}	1.6×10^{-4}	1.9×10^{-4}
IODP X311	U1327C	210.6	29.0	1.2	0.78	1675	90 (?)	−1585	0.05	0.18	0.02	1.2×10^{-4}	1.2×10^{-4}	5.0×10^{-4}
IODP X311	U1329C	21.85	50.0	1.37	0.79	145	175	30	1.21	0.47	0.07	2.0×10^{-7}	2.0×10^{-7}	1.8×10^{-7}
IODP X311	U1329C	32.85	46.0	1.32	0.84	231	485	254	2.10	0.53	0.07	5.0×10^{-7}	3.1×10^{-7}	2.9×10^{-7}
IODP X311	U1329C	131.85	40.0	1.44	1.05	918	1180	262	1.29	0.76	0.07	9.0×10^{-5}	7.0×10^{-5}	1.2×10^{-5}
IODP X311	U1329C	146.15	45.0	1.64	1.17	1038	500	−538	0.48	0.63	0.11	2.0×10^{-6}	6.0×10^{-7}	1.0×10^{-7}
IODP X311	U1329C	165.07	37.0	1.69	1.34	1159	550	−609	0.47	0.46	0.11	4.0×10^{-6}	2.5×10^{-6}	5.0×10^{-6}
ODP Leg 164	995A	3.09	76.0	2.01		14	40	26	2.90	0.67				
ODP Leg 164	995A	49.57	95.4	2.53		270	205	−65	0.76	1.38				
ODP Leg 164	995A	148.48	64.9	1.72		885	430	−455	0.49	0.94				
ODP Leg 164	995A	253.4	54.2	1.44		1610	400	−1210	0.25	0.68				
ODP Leg 164	995A	350.8	54.2	1.44		2350	780	−1570	0.33	0.69				
ODP Leg 164	995A	467	49.9	1.36		3290	1770	−1520	0.54	0.93				
ODP Leg 164	995A	546.11	65.3	1.73		3940	1330	−2610	0.34	0.97				
ODP Leg 164	995A	666.85	57.3	1.52		4970	2730	−2240	0.55	0.93				

virgin compression portion of some curves is subject to multiple interpretations, possibly the result of sample disturbance. Although there is significant variation among tests, the mean C_c for all tests (0.69) is remarkably close to the mean C_c (0.67) predicted from LL values (Bowles, 1979) for each sample. Rebound compression indices ranged from 0.02 to 0.18. The low c_v values at in situ stress reflect the fine-grained nature of the sediment.

The underconsolidated behavior (OCR<1) of the deeper NGHP-01 sediment is consistent with a previous study conducted on ODP Leg 164 sediment (OCR in Table 9, Fig. 16) from the Blake Ridge (Winters et al., 2000b). Underconsolidation, due to rapid sedimentation, was hypothesized to occur at the Blake Ridge (Hyndman and Davis, 1992), an area containing widespread gas hydrate deposits (Dillon et al., 1980; Dillon and Kvenvolden, 1982). Underconsolidation may be one of the mechanisms for bringing additional methane into the hydrate stability zone (Hyndman and Davis, 1992) through fluid flow, which is necessary for the formation of significant gas hydrate deposits (Ginsburg and Soloviev, 1997; Judd and Hovland, 2007; Xu and Ruppel, 1999).

4.2.5. Triaxial strength properties

Both undrained and drained strength parameters are used in different types of models to predict in situ behavior under certain loading conditions. Performing undrained strength tests with pore-pressure measurement enables both types of strength parameters to be calculated. Results of triaxial shear strength tests on sediments recovered from marine (NGHP-01 and ODP Leg 204) and permfrost-associated (Mallik 2L) gas hydrate provinces show significant

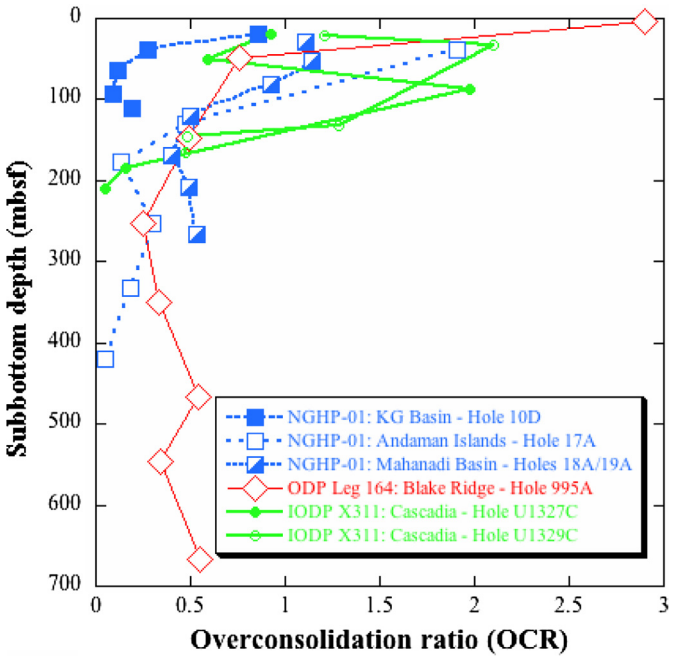

Figure 16. Overconsolidation ratio (OCR) versus subbottom depth for sediment samples from the NGHP-01, IODP X311, and ODP Leg 164 projects.

Table 10
Triaxial strength results for the NGHP-01, ODP Leg 204, and Mallik 2L-38 projects. (*) Although undrained tests were performed, the coarse-grained nature of the sediment indicates that drained strength parameters will probably govern behavior.

General information														
Project	NGHP-01 (India)	NGHP-01 (India)	NGHP-01 (India)	NGHP-01 (India)	NGHP-01 (India)	NGHP-01 (India)	NGHP-01 (India)	NGHP-01 (India)	NGHP-01 (India)	ODP Leg 204	Mallik 2L-38	Mallik 2L-38	Mallik 2L-38	Mallik 2L-38
Region	KG Basin	KG Basin	KG Basin	KG Basin	KG Basin	KG Basin	Mahanadi Basin	Mahanadi Basin	Mahanadi Basin	Cascadia - Hydrate Ridge	Mackenzie Delta, NWT, Canada	Mackenzie Delta, NWT, Canada	Mackenzie Delta, NWT, Canada	Mackenzie Delta, NWT, Canada
Hole	21A	21A	21A	10D	10D	10D	18A	18A	18A	1249	Mallik-2L	Mallik-2L	Mallik-2L	Mallik-2L
Section	2Y (Fugro pressure core)	2Y (Fugro pressure core)	2Y (Fugro pressure core)	10X	10X	10X	5H	5H	5H	4H				
Subbottom depth interval (m)	58.44	58.04	58.24	64.02	64.02	64.02	40.15	40.15	40.15	26.53	913	913.13	898.97	899.23
Index properties														
Water content Initial (Msw/Ms) (%)	54.8	58.26	60.8	60.7	59.4	57.9	58.8	58.4	57.9	65.2	21.3	20.6	15.5	17.9
Water content Pre-shear (Msw/Ms) (%)	37.8	47.34	50.5	56.3	45.1	38.3	58.1	51.3	46.5					
Porosity (calc.) Initial (%)	59.1	60.7	61.7							62.9	37.2	36.5	30.0	33.0
Porosity (calc.) Pre-shear (%)	52.6	55.5	57.3											
Void ratio Initial				1.79	1.74	1.70	1.64	1.63	1.70	1.69				
Void ratio Pre-shear				1.57	1.25	1.06	1.62	1.43	1.29					
Grain size														
Gravel//Sand//Silt//Clay-size										0//0.8//56.5//42.7	3.2//93.1//2.5//1.2	3.6//92.7//2.5//1.3	0//91.9//6.9//1.2	0//92.9//5.6//1.4
Mean (phi)	5.92	8.31	8.74							7.75				
Median (phi)	6.08	9.60	9.98											
Mean/Median ratio	0.97	0.87	0.87											
Standard Deviation	3.35	3.53	3.87											
Skewness	0.00	−0.25	−0.18											
Kurtosis	−0.73	−0.83	−0.84											
Shear properties														
Pore contents at shear	Water	Water	Water	Water	Water	Water	Water	Water	Water	Water	Water	Water	Water	Gas hydrate
Consolidation stress (kPa)	399.04	408.45	416.81	40	310	620	30	189	380	970	240	220	260	360
Strain rate (%/hour)	0.129	0.139	0.142	0.96	0.96	0.96	0.96	0.96	0.96					
A (failure)	0.65	0.604	1.08	0.96	0.95	1.02	0.22	0.84	0.98	1.12	−0.33	−0.31	−0.26	−0.26
q (failure) (kPa)	172.76	176.75	118.51	12.5	94.1	166.8	26.3	69.9	111.9	297	1550	1380	820	6690
p' (failure) (kPa)	347.37	371.81	279.98							612	2800	2450	1530	10540
q/p' ratio	0.433	0.43	0.284	0.31	0.30	0.27	0.88	0.37	0.29	0.31	6.5*	6.2*	3.2*	18.6*
Axial strain (failure) (%)	10.0	5.7	13.8	2.1	7.1	8.0	8.5	8.7	4.9	14.5	15.0	13.4	15.0	8.8
ϕ'max, friction angle (deg.)	30.16	30.95	25.2							29.0	37.5	38.6	33.8	44.4
ϕ', composite friction angle (deg.)				21.3	21.3	21.3	24.5	24.5	24.5					
c' kPa				7.2	7.2	7.2	9.7	9.7	9.7					

differences between fine- and coarse-grained sediment behavior (Table 10) (Winters et al., 1999b; Winters et al., 2004; Winters et al., 2006; Winters et al., 2007d; Winters et al., 2008b). The fine-grained marine samples exhibited contractive behavior (positive "A" coefficient at failure) and stress paths that bend to the left during shear. The "A" coefficients are within or close to the range of 0.7–1.3 for normally consolidated clays (Bowles, 1979). The coarse-grained permafrost-related Arctic sediment exhibited dilative behavior (negative "A" coefficient). However, this may also be due to the application of lower consolidation stresses (Table 10). Normally consolidated undrained strength to consolidation stress ratios (S_u/p') (also q/p') (0.27, 0.28, 0.29, 0.31, 0.43, 0.43) were higher than the typically assumed value of 0.22 for clayey sediment (Mesri, 1989), however, values can range from 0.09 to 0.35 (Bowles, 1979). NGHP-01-10D and -18A Su/p' values (0.27 and 0.29) are nearly identical to the predicted values of 0.29 and 0.30 based on plasticity index (Bowles, 1979). Composite friction angles ranged from 21.3 to 24.5° for NGHP-01 Holes 10D and 18A. These are within the range of 25° for "undisturbed" clay to 17° for remolded clay (Bjerrum and Simons, 1960). Clayton et al. (2008) suggest that friction angles for sediment from Hole NGHP-01-10B should be within the range of 20–30°, although they measured maximum values of 26° and 34° (c' equal to 0). As expected, the sandy sediments from the Mackenzie Delta (Mallik) (Table 10) had higher friction angles (assuming no cohesion intercept) between 33.8 and 44.4°.

5. Summary

Physical properties of sediment from NGHP-01, IODP X311, four other marine, and three permafrost-related Arctic field study areas provide valuable insight into the intrinsic nature and behavior of sediment that may host or be adjacent to gas-hydrate deposits. Grain size, index, well-log, magnetic, electrical resistivity, thermal, acoustic velocity, constant-rate-of-strain consolidation, and strength properties are presented. Although all properties are interrelated, to some extent, some measurements correlate better to the presence of gas hydrate, while other measurements can be used to predict sediment behavior under different loading conditions. Geotechnical test programs should include a subset from each of the major test types, if possible. Whether gas hydrate is present in the sediment during testing is critical to deciding which properties should be measured. For example, electrical resistivity and acoustic velocity would be important if hydrate was present, whereas grain size and other index properties would be appropriate after dissociation. Consolidation and strength measurements should be included as appropriate.

Properties of individual wells drilled during NGHP-01 are discussed in detail. In addition, regional NGHP-01 trends are also compared. Grain-size, porosity, and permeability patterns are responsible for a host of intrinsic behavioral differences that have a direct impact on gas migration prior to hydrate formation. Furthermore, coarse grain size profoundly affects the suitability of sediment to host high pore-filling gas-hydrate saturations. Over 2000 analyses, performed as part of the NGHP-01 and other expeditions, show the critical relationship between grain size and in situ occurrences of gas hydrate as constrained by well logs. In fine-grained sediments around the world, gas hydrate typically is present at low pore saturations. However, in fractured reservoirs, it is still the host properties that influence fracture patterns, both locally and regionally, that enable (a) the formation of high concentrations of hydrates, such as at Hole NGHP-01-10D and (b) regional transport of fluids and gases to the hydrate stability zone. Most sediment recovered during NGHP-01 is fine grained, but coarse grained sections associated with channel deposits (e.g., Hole NGHP-01-15A) are host to higher hydrate saturations. The upper sections of most holes follow typical compaction trends for marine sediments, but the lower sections of Holes NGHP-01-17A and -19A show little change in porosity with depth, possibly related to higher siliceous content of the biogenic sediment and underconsolidation.

Index properties, including Atterberg limits, are generally consistent with and provide a means to predict and corroborate more advanced consolidation and triaxial strength testing. Consolidation testing indicates that pseudo-overconsolidated sediment nearer the seafloor is underlain by underconsolidated sediment at depth offshore India in the KG Basin, Mahanadi Basin, and offshore the Andaman Islands. This may be the result of rapid sedimentation or inherent physical sediment characteristics (for example, nannofossil ooze near the Andaman Islands). Triaxial strength parameters, including S_u/p' ratio, "A" coefficient, and friction angles, for NGHP-01 kG and Mahanadi Basins, are all in close agreement to predicted values based on plasticity characteristics of the tested sediment, indicating that standard geotechnical relationships may be appropriate to use for estimating properties and predicting behavior.

Gas hydrate morphology offshore India, on the Cascadia continental margin, and in the Gulf of Mexico is typically more complex than in the few permafrost-related Arctic locations that have been sampled. The hydrate complexity is related primarily to widespread, but not exclusively, finer-grained deposits offshore. In wells off the east coast of India, GH was present in sand-rich, fractured clay, and in reservoirs with both characteristics. At Site NGHP-01-10, in the Krishna-Godavari Basin, GH was observed in several morphologic configurations, including complex high-angle planar and rotational veins, solid nodules, and disseminated. Sediment in a well off the Andaman Islands sporadically hosted disseminated GH in thin coarser-grained ash beds and ash-rich zones. Sandy GH reservoirs are not only associated with Arctic permafrost, but are also found offshore, e.g., Nankai Trough, off the Andaman Islands, Site NGHP-01-15 in the KG Basin, Cascadia, and the Gulf of Mexico.

Within two permafrost-related gas hydrate areas, the Mount Elbert well on the Alaskan North Slope and the Mallik wells on the Mackenzie Delta, NWT, >10-m thick gas hydrate-bearing sandy deposits are capped by finer-grained sediments that may reduce gas migration. A sandier section in NGHP-01-15A is also bounded by finer-grained sediment. Within the coarse-grained sediments, gas hydrate typically has a pore-filling characteristic. At the Mount Elbert well, the grain size distributions of hydrate-bearing layers and respective "seals" are significantly different.

Collectively, the results enhance our understanding of sedimentation, geologic stress history, and hydrate occurrence in geologically complex deposits containing fine- and coarse-grained sediment. These properties, in conjunction with well logs and other field measurements, provide the means for assessing geologic controls on the location of gas hydrate and predicting behavior of host formations during exploratory drilling or production operations.

Acknowledgments

The authors wish to thank those that contributed to the success of the National Gas Hydrate Program Expedition 01 (NGHP01). NGHP01 was planned and managed through collaboration between the Directorate General of Hydrocarbons (DGH) under the Ministry of Petroleum and Natural Gas (India), the U.S. Geological Survey (USGS), and the Consortium for Scientific Methane Hydrate Investigations (CSMHI) led by Overseas Drilling Limited (ODL) and FUGRO McClelland Marine Geosciences (FUGRO). The platform for the drilling operation was the research drill ship JOIDES Resolution, operated by ODL. Much of the drilling/coring equipment used was provided by the Integrated Ocean Drilling Program (IODP) through

a loan agreement with the US National Science Foundation. Wireline pressure coring systems and supporting laboratories were provided by IODP/Texas A&M University (TAMU), FUGRO, USGS, U.S. Department of Energy (USDOE) and HYACINTH/GeoTek. Downhole logging operational and technical support was provided by Lamont-Doherty Earth Observatory (LDEO) of Columbia University. The financial support for the NGHP01, from the Oil Industry Development Board, Oil and Natural Gas Corporation Ltd., GAIL (India) Ltd. and Oil India Ltd. is gratefully acknowledged. We also acknowledge the support extended by all the participating organizations of the NGHP: MoP&NG, DGH, ONGC, GAIL, OIL, NIO, NIOT, and RIL.

Carolyn Ruppel and two anonymous reviewers provided helpful comments. Robert Cannata, Maya Gomes, Kate McMullen, and Rebecca Sorell performed the grain-size analyses. Geotechnical tests for NGHP-01 and IODP X311 samples were performed at GeoTesting Express, Inc., Boxboro, MA by Nancy Hubbard under the supervision of Gary Torosian and Joe Tomei. Mike Driscoll also performed some of the constant-rate-of-strain consolidation tests. H. Todd Schaef performed and processed infrared measurements at sea. Wylie Poag and Jason Chaytor helped interpret SEM images. The drillers and various field staff are thanked for obtaining cores, performing logging runs, and providing logistical support under adverse conditions. Dave Mason fabricated the pressure hoses and prepared other physical-property-related supplies used at sea. The NGHP-01 and other programs discussed in this paper would never have been possible without the leadership and assistance of Tim Collett. This work was supported by the Coastal and Marine Geology, and Energy Programs of the U.S. Geological Survey. Partial support for this research was provided by Interagency Agreement DE-FE0002911 between the USGS Gas Hydrates Project and the U.S. Department of Energy's Methane Hydrates R&D Program.

The datasets contained in this report have been approved for release and publication by the USGS. Although these datasets have been subjected to rigorous review and are substantially complete, the USGS reserves the right to revise the data pursuant to further analysis and review. Furthermore, they are released on condition that neither the USGS nor the United States Government may be held liable for any damages resulting from their authorized or unauthorized use.

Any use of trade, product, or firm names is for descriptive purposes only and does not imply endorsement by the U.S. Government.

References

American_Society_for_Testing_and_Materials, 1997. Standard test method for specific gravity of solids by gas pycnometer D5550-94. In: Annual Book of ASTM Standards, v. 04.09, Soil and Rock. American Society for Testing and Materials, West Conshohocken, Pennsylvania, pp. 380–383.

American_Society_for_Testing_and_Materials, 2006. Standard test methods for laboratory determination of water (moisture) content of soil and rock by mass D2216-05. In: Annual Book of ASTM Standards, v. 04.08, Soil and Rock. American Society for Testing and Materials, West Conshohocken, Pennsylvania, pp. 205–211.

American_Society_for_Testing_and_Materials, 2008a. Standard practice for description and identification of soils (visual-manual procedure) D 2488. In: Annual Book of ASTM Standards, v. 04.08, Soil and Rock. American Society for Testing and Materials, West Conshohocken, Pennsylvania, pp. 272–282.

American_Society_for_Testing_and_Materials, 2008b. Standard test method for one-dimensional consolidation properties of saturated cohesive soils using controlled-strain loading D 4186. In: Annual Book of ASTM Standards, v. 04.08, Soil and Rock. American Society for Testing and Materials, West Conshohocken, Pennsylvania, pp. 520–534.

American_Society_for_Testing_and_Materials, 2008c. Standard test methods for liquid limit, plastic limit, and plasticity index of soils D 4318. In: Annual Book of ASTM Standards, v. 04.08, Soil and Rock. American Society for Testing and Materials, West Conshohocken, Pennsylvania, pp. 581–596.

ASTM, 2010. Standard test method for consolidated undrained triaxial compression test for cohesive soils D 4767. In: Annual Book of ASTM Standards, v. 04.08, Soil and Rock. American Society for Testing and Materials, West Conshohocken, Pennsylvania, pp. 932–944.

Atkinson, J., 1993. An Introduction to the Mechanics of Soils and Foundations Through Critical State Soil Mechanics. McGraw-Hill Book Company, London, p. 337.

Bishop, A.W., Henkle, D.J., 1962. The Measurement of Soil Properties in the Triaxial Test. Edward Arnold (Publishers) LTD, London, p. 227.

Bjerrum, L., Simons, N.E., 1960. Comparison of shear strength characteristics of normally consolidated clays. In: Proceedings 1st PSC, pp. 711–726.

Blum, P., 1997. Physical Properties Handbook: a Guide to the Shipboard Measurement of Physical Properties of Deep-sea Cores. ODP Technical Note 26. http://www-odp.tamu.edu/publications/tnotes/tn26/INDEX.HTM [cited 2007-05-11].

Bohrmann, G., Greinert, J., Suess, E., Torres, M., 1998. Authigenic carbonates from the Cascadia subduction zone and their relation to gas hydrate stability. Geol. (Boulder) 26 (7), 647–650.

Boswell, R., Collett, T.S., 2011. Current perspectives on gas hydrate resources. Energy & Environ. Sci. 4 (4), 1206.

Boswell, R., Collett, T.S., Frye, M., Shedd, W., McConnell, D.R., Shelander, D., 2012. Subsurface gas hydrates in the northern Gulf of Mexico. Mar. Pet. Geol. 34 (1), 4–30.

Bowles, J.E., 1979. Physical and Geotechnical Properties of Soils. McGraw-Hill Book Company, New York, p. 478.

Boyce, R.E., 1968. Electrical resistivity of modern Marine sediments from the Bering sea. J. Geophys. Res. 73 (14), 4759–4766.

Bryant, W.R., Trabant, P.K., 1972. Statistical relationships between geotechnical properties of Gulf of Mexico sediments. In: Proceedings 4th Annual Offshore Technology Conference, Dallas, 1654, pp. 363–368. OTC Paper Number.

Busch, W.H., 1989. Patterns of sediment compaction at ocean drilling program sites 645,646, and 647, Baffin Bay and Labrador sea. In: Proceedings of the Ocean Drilling Program, Scientific Results, vol. 105, pp. 781–790.

Carmichael, R.S., 1982. Handbook of Physical Properties of Rocks. CRC Press, Inc., Boca Raton, FL, p. 345.

Casagrande, A., 1936. The determination of the pre-consolidation load and its practical significance. In: Proceedings First International Conference on Soil Mechanics and Foundation Engineering, 3. Harvard University, Cambridge, MA, pp. 60–64.

Clark, D.A., Emerson, D.W., 1991. Notes on rock magnetization characteristics in applied geophysical studies. Explor. Geophys. 22, 547–555.

Claypool, G.E. (Ed.), 2006. Cruise Report: the Gulf of Mexico Gas Hydrate Joint Industry Project. http://www.netl.doe.gov/technologies/oil-gas/publications/Hydrates/reports/GOMJIPCruise05.pdf [cited 2007-04-12].

Clayton, C., Kingston, E., Priest, J., Schultheiss, P., 2008. Testing of pressurized cores containing gas hydrate from deep ocean sediments. In: Proceedings 6th International Conference on Gas Hydrates, Vancouver, B.C.

Clennell, M.B., Hovland, M., Booth, J.S., Henry, P., Winters, W.J., 1999. Formation of natural gas hydrates in marine sediments: 1. Conceptual model of gas hydrate growth conditioned by host sediment properties. J. Geophys. Res. 104 (B10), 22985.

Collett, T., Johnson, A., Knapp, C., Boswell, R., 2009. Natural Gas Hydrates – Energy Resource Potential and Associated Geologic Hazards. In: AAPG Memoir 89. American Association of Petroleum Geologists, p. 145.

Collett, T., Riedel, M., Cochran, J., Boswell, R., Presley, J., Kumar, P., Sathe, A., Sethi, A., Lall, M., Sibal, V., 2008a. Indian National Gas Hydrate Program Expedition 01 Initial Reports. Directorate General of Hydrocarbons.

Collett, T.S., 1995. Gas Hydrate Resources of the United States: Natl Assessment of US Oil & Gas Resources (CD-ROM). In: Gautier, D.L., Dolton, G.L. (Eds.), USGS Ser, vol. 30, p. 78.

Collett, T.S., 2002. Energy resource potential of natural gas hydrates. AAPG Bull. 86 (11), 1971–1992.

Collett, T.S., 2008. Arctic gas hydrate energy assessment studies. In: Proceedings the Arctic Energy Summit, Anchorage, AK. Institute of the North, pp. 1–12.

Collett, T.S., et al., 2014. Scientific Results of the National Gas Hydrate Program Expedition (in this volume).

Collett, T.S., Lee, M.W., Agena, W.F., Miller, J.J., Lewis, K.A., Zyrianova, M.V., Boswell, R., Inks, T.L., 2011. Permafrost-associated natural gas hydrate occurrences on the Alaska North Slope. Mar. Pet. Geol. 28 (2), 279–294.

Collett, T.S., Lewis, R.E., Dallimore, S.R., Lee, M.W., Mroz, T.H., Uchida, T., 1999. Detailed evaluation of gas hydrate reservoir properties using JAPEX/JNOC/GSC Mallik 2L-38 gas hydrate research well downhole well-log displays. Bull. – Geol. Surv. Can. Report 544, 295–311.

Collett, T.S., Riedel, M., Cochran, J.R., Boswell, R., Kumar, P., Sathe, A.V., party, N. E. s, 2008b. Indian continental margin gas hydrate prospects: results of the Indian National Gas Hydrate Program (NGHP) expedition 01. In: Proceedings 6th International Conference on Gas Hydrates, Vancouver, British Columbia, Canada, July 6–10, 2008.

Cook, A., Goldberg, D., 2008a. Extent of gas hydrate filled fracture planes: implications for in situ methanogenesis and resource potential. Geophys. Res. Lett. 35.

Cook, A., Goldberg, D., 2008b. Stress and gas hydrate-filled fracture distribution, Krishna–Godavari Basin, India. In: Proceedings 6th International Conference on Gas Hydrates, Vancouver, B.C., July 6–10, 2008.

Cook, A.E., Anderson, B.I., Malinverno, A., Mrozewski, S., Goldberg, D.S., 2010. Electrical anisotropy due to gas hydrate-filled fractures. Geophysics 75 (6), F173–F185.

Cooper, A.K., Hart, P.E., 2003. High-resolution seismic-reflection investigation of the northern Gulf of Mexico gas-hydrate-stability zone. Mar. Pet. Geol. 19 (10), 1275–1293.

Dai, S., Santamarina, J.C., Waite, W.F., Kneafsey, T.J., 2012. Hydrate morphology: physical properties of sands with patchy hydrate saturation. J. Geophys. Res. 117 (B11).
Dallimore, S.R., Collett, T.S., 2005. Summary and implications of the Mallik 2002 gas hydrate production research well program. In: Dallimore, S.R., Collett, T.S. (Eds.), Scientific Results from the Mallik 2002 Gas Hydrate Production Research Well Program, Mackenzie Delta, Northwest Territories, 585. Geological Survey of Canada, Bulletin, Canada, Ottawa, pp. 1–36.
Dallimore, S.R., Collett, T.S., Uchida, T., 1999a. Summary–Sommaire. Bull. – Geol./Surv. Can. Report 544, 1–10.
Dallimore, S.R., Uchida, T., Collett, T.S., 1999b. Scientific Results From JAPEX/JNOC/GSC Mallik 2L-38 Gas Hydrate Research Well, Mackenzie Delta, Northwest Territories, 544. Geological Survey of Canada, Bulletin, Canada, Ottawa, p. 403.
Davis, E.E., Hyndman, R.D., Villinger, H., 1990. Rates of fluid expulsion across northern Cascadia accretionary prism: constraints from new heat flow & multichannel seismic reflection data. J. Geophys. Res. 95 (B6), 8869–8889.
Dillon, W.P., Grow, J.A., Paull, C.K., 1980. Unconventional gas hydrate seals may trap gas off Southeast U.S. Oil Gas. J. 78 (1), 124–130.
Dillon, W.P., Kvenvolden, K.A., 1982. Gas hydrates in sea floor sediments off Southeastern United States: evidence from seismic reflection and drilling data. In: Proceedings Methane Hydrates Workshop Technical Proceedings, Morgantown, WV, March 29–30, 1982, p. 78.
Esteban, L., Enkin, R.J., Hamilton, T., 2008. Gas hydrates and magnetism: comparative geological settings for diagenetic analysis. In: Proceedings 6th International Conference on Gas Hydrates, Vancouver, B.C, p. 9.
Francisca, F., Yun, T.S., Ruppel, C., Santamarina, J.C., 2005. Geophysical and geotechnical properties of near-seafloor sediments in the northern Gulf of Mexico gas hydrate province. Earth Planet. Sci. Lett. 237 (3–4), 924–939.
Geotek, L., 2000. Multi-sensor Core Logger.
Ghosh, R., Sain, K., Ojha, M., 2010. Effective medium modeling of gas hydrate-filled fractures using the sonic log in the Krishna-Godavari basin, offshore eastern India. J. Geophys. Res. 115 (B06101).
Ginsburg, G.D., Soloviev, V.A., 1997. Methane migration within the submarine gas-hydrate stability zone under deep-water conditions. Mar. Geol. 137 (1–2), 49–57.
Hamilton, E., 1976. Variations of density and porosity with depth in deep-sea sediments. J. Sediment. Pet. 46 (2), 280–300.
Holland, M., Schultheiss, P., Roberts, J., Druce, M., 2008. Observed gas hydrate morphologies in marine sediments. In: Proceedings 6th International Conference on Gas Hydrates, Vancouver, B.C., Canada, July 6–10, 2008.
Holtz, R.D., Kovacs, W.D., 1981. An Introduction to Geotechnical Engineering. Prentice-Hall, Inc., Englewood Cliffs, NJ, p. 733.
Huey, D.P., 2009. IODP Drilling and Coring Technology – Past and Present – Phase 2: Final Report. Presented to IODP-MI from Stress Engineering Services, Inc., p. 183.
Hunt, R.E., 1984. Geotechnical Engineering Investigation Manual. McGraw-Hill Book Company, New York, NY, p. 983.
Hunter, R.B., Collett, T.S., Boswell, R., Anderson, B.J., Digert, S.A., Pospisil, G., Baker, R., Weeks, M., 2011. Mount Elbert Gas hydrate stratigraphic test well, Alaska North slope: overview of scientific and technical program. Mar. Pet. Geol. 28 (2), 295–310.
Hunter, R.B., Digert, S.A., Boswell, R., Collett, T.S., 2008. Alaska gas hydrate research and stratigraphic test preliminary results. In: Proceedings the Arctic Energy Summit, Anchorage, AK.
Hutchinson, D., Shelander, D., Latham, T., McConnell, D., Ruppel, C., Jones, E., Boswell, R., Shedd, W., Frye, M., 2008a. Site selection for DOE/JIP gas hydrate drilling in the northern Gulf of Mexico. In: Proceedings 6th International Conference on Gas Hydrates, Vancouver, B.C., July 6–10, 2008, pp. 66–67. Volume Final Program and Book of Abstracts.
Hutchinson, D.R., Hart, P.E., Collett, T.S., Edwards, K.M., Twichell, D.C., Snyder, F., 2008b. Geologic framework of the 2005 Keathley Canyon gas hydrate research well, northern Gulf of Mexico. Mar. Pet. Geol. 25 (9), 906–918.
Hyndman, R.D., Davis, E.E., 1992. A mechanism for the formation of methane hydrate and seafloor bottom-simulating reflectors by vertical fluid expulsion. J. Geophys. Res. 97 (B5), 7025–7041.
Judd, A., Hovland, M., 2007. Seabed Fluid Flow the Impact on Geology, Biology, and the Marine Environment. Cambridge University Press, Cambridge, U.K.
Keller, G., 1974. Marine geotechnical properties: interrelationships and relationships to depth of burial. In: Inderbitzen, A. (Ed.), Deep Sea Sediments. Plenum Publishing Corporation, New York, pp. 77–100.
Kelly, R.N., DiSante, K.J., Stranzl, E., Kazanjian, J.A., Bowen, P., Matsuyama, T., Gabas, N., 2006. Graphical comparison of image analysis and laser diffraction particle size analysis data obtained from the measurements of nonspherical particle systems. AAPS PharmSciTech 7 (3).
Kim, Y.J., Yun, T.S., 2013. Thermal conductivity of methane hydrate-bearing Ulleung Basin marine sediments: laboratory testing and numerical evaluation. Mar. Pet. Geol. 47, 77–84.
Kraemer, L.M., Owen, R.M., Dickens, G.R., 2000. Lithology of the upper gas hydrate zone, Blake Outer Ridge: a link between diatoms, porosity, and gas hydrate. In: Proceedings of the Ocean Drilling Program: Scientific Results, vol. 164, pp. 229–236.
Kumar, P., Collett, T.S., Sethi, A.K., Sathe, A.V., Sibal, V.K., Riedel, M., Boswell, R., Cochran, J.R., Party, N.E.-S., 2007. Gas hydrate coring/drilling program in Indian offshore – an overview of NGHP Expedition-01, 2006. In: Proceedings PETROTECH-2007, New Delhi, India, January 15–19, 2007. Oil and Natural Gas Corporation.
Lambe, T.W., Whitman, R.V., 1969. Soil Mechanics. John Wiley & Sons, New York, p. 553.
Lee, J.Y., Kim, G.Y., Kang, N.K., Yi, B.Y., Jung, J.W., Im, J.H., Son, B.K., Bahk, J.J., Chun, J.H., Ryu, B.J., Kim, D.S., 2013. Physical properties of sediments from the Ulleung Basin, east sea: results from second Ulleung Basin Gas hydrate drilling expedition, east sea (Korea). Mar. Pet. Geol. 47, 43–55.
Lee, M.W., Collett, T.S., 2009a. Gas hydrate saturations estimated from fractured reservoir at Site NGHP-01-10, Krishna-Godavari Basin, India. J. Geophys. Res. 114 (B7).
Lee, M.W., Collett, T.S., 2009b. Gas hydrate saturations estimated from fractured reservoir at Site NGHP-01-10, Krishna-Godavari Basin, India. J. Geophys. Res.-Solid Earth 114.
Lee, M.W., Collett, T.S., 2011. In-situ gas hydrate hydrate saturation estimated from various well logs at the Mount Elbert Gas Hydrate Stratigraphic Test Well, Alaska North Slope. Mar. Pet. Geol. 28 (2), 439–449.
Long, P., Holland, M., Schultheiss, P., Riedel, M., Weinberger, J., Tréhu, A., Schaef, H., 2010. Infrared imaging of Gas-Hydrate-Bearing cores: state of the art and future prospects. In: Riedel, M., Willoughby, E., Satinder, C. (Eds.), Geophysical Characterization of Gas Hydrates. Society of Exploration Geophysicists, pp. 217–232.
Long, P.E., Rose, K.K., Schaef, H.T., Torres, M.E., Solomon, E.A., Kastner, M., Johnson, J.E., Giosan, L., Winters, W.J., Dewri, S., Kumar, P., 2009. Gas hydrate occurrence in marine sediments and volcanic ash of the Andaman arc: results from NGHP Expedition 01, Site 17. In: Proceedings 237th American Chemical Society National Meeting, Division of Fuel Chemistry, Salt Lake City, UT, March 22–26, 2009, pp. 135–136.
Lorenson, T.D., Winters, W.J., Hart, P.E., Paull, C.K., 2002. Gas hydrate occurrence in the northern Gulf of Mexico studied with giant piston cores. Eos Trans. Am. Geophys. Union 83 (51), 601.
MacDonald, I.R., Leifer, I., Sassen, R., Stine, P., Mitchell, R., Guinasso Jr., N., 2002. Transfer of hydrocarbons from natural seeps to the water column and atmosphere. Geofluids 2 (2), 95–107.
Marr, W.A., 2002. State of the practice: geotechnical laboratory testing. In: Proceedings XVII Seminario Venezolano de Geotecnia, “Del Estado del Arte a la Práctica”, p. 23.
Mesri, G., 1975. Discussion of New design procedures for stability of soft clays. J. Geotech. Eng. Div. ASCE 101 (GT4), 409–412.
Mesri, G., 1989. A reevaluation of su = 0.22 σ'v using laboratory shear tests. Can. Geotech. J. 162–164.
Minor, S.A., Hudson, M.R., 2006. Regional Survey of Structural Properties and Cementation Patterns of Fault Zones in the Northern Part of the Albuquerque Basin, New Mexico - Implications for Ground-water Flow.
Paull, C.K., Matsumoto, R., Wallace, P., Black, N.R., Borowski, W.S., Collett, T.S., Damuth, J.E., Dickens, G.R., Egeberg, P.K., Goodman, K., Hesse, R.F., Hiroki, Y., Holbrook, W.S., Hoskins, H., Ladd, J., Lodolo, E., Lorenson, T.D., Musgrave, R.J., Naehr, T., Okada, H., Pierre, C., Ruppel, C.D., Satoh, M., Thiery, R., Watanabe, Y., Wehner, H., Winters, W.J., Wood, W.T., Pollard, E., Hohnberg, H.-J., Kawasaki, M., Kittredge, S., Meltser, A., Stahl, M., Kittrege, S., 1996. Introduction. In: Proceedings of the Ocean Drilling Program, Part a: Initial Reports, 164, pp. 5–12.
Poppe, L.J., Elisaon, A.H., Hastings, M.E., 2004. A visual basic program to generate grain-size statistics and to extrapolate particle distributions. Comput. Geosci. 30, 791–795.
Poppe, L.J., Williams, S.J., Paskevich, V.F., 2005. U.S. Geological Survey East-coast Sediment Analysis: Procedures, Database, and GIS Data, U.S. Geological Survey Open-File Report 2005–1001.
Priest, J., Kingston, E., Clayton, C., Schultheiss, P., Druce, M., 2008. The structure of hydrate bearing fine grained marine sediments. In: Proceedings 6th International Conference on Gas Hydrates, Vancouver, B.C, p. 8.
Ratcliffe, E.H., 1960. The thermal conductivities of ocean sediments. J. Geophys. Res. 65, 1535–1541.
Rees, E.V.L., Priest, J.A., Clayton, C.R.I., 2011. The structure of methane gas hydrate bearing sediments from the Krishna–Godavari Basin as seen from Micro-CT scanning. Mar. Pet. Geol. 28 (7), 1283–1293.
Riedel, M., Collett, T.S., Kumar, P., Sathe, A.V., Cook, A., 2010a. Seismic imaging of a fractured gas hydrate system in the Krishna-Godavari Basin offshore India. Mar. Pet. Geol. 27 (7), 1476–1493.
Riedel, M., Collett, T.S., Malone, M.J., 2010b. Expedition 311 synthesis: scientific findings. In: Proceedings of the Integrated Ocean Drilling Program, vol. 311, pp. 1–28. http://dx.doi.org/10.2204/iodp.proc.311.213.2010.
Riedel, M., Collett, T.S., Shankar, U., 2011. Documenting channel features associated with gas hydrates in the Krishna–Godavari Basin, offshore India. Mar. Geol. 279 (1–4), 1–11.
Robertson, J., Hakun, J., Gillette, C., 2013. New Insight on Gas Hydrates in Gulf of Mexico, USGS Newsroom Technicl Announcement. Geological Survey, Reston, VA, U.S.
Rose, K., Boswell, R., Collett, T., 2011. Mount Elbert Gas hydrate stratigraphic test well, Alaska North slope: coring operations, core sedimentology, and lithostratigraphy. Mar. Pet. Geol. 28 (2), 311–331.
Rose, K., Johnson, J., Torres, M., Solomon, E., Long, P., Kastner, M., Schaef, H., Giosan, L., 2014. Preferential accumulation of gas hydrate in porous-permeable volcanic ash beds of the Andaman Arc. Mar. Pet. Geol. (in this issue).
Ruppel, C., Boswell, R., Jones, E., 2008. Scientific results from gulf of Mexico Gas hydrates joint Industry project leg 1 drilling: introduction and overview. Mar. Pet. Geol. 25 (9), 819–829.
Ruppel, C., Dickens, G.R., Castellini, D.G., Gilhooly, W., Lizarralde, D., 2005. Heat and salt inhibition of gas hydrate formation in the northern Gulf of Mexico. Geophys. Res. Lett. 32 (L04605) http://dx.doi.org/10.1029/2004GL021909.

Shankar, U., Riedel, M., 2011. Gas hydrate saturation in the Krishna–Godavari basin from P-wave velocity and electrical resistivity logs. Mar. Pet. Geol. 28 (10), 1768–1778.
Shepard, F.P., 1954. Nomenclature based on sand-silt-clay ratios. J. Sediment. Petrol. 24, 151–158.
Stern, L.A., Kirby, S.H., 2008. Natural gas hydrates up close: a comparison of grain characteristics of samples from marine and permafrost environments as revealed by cryogenic SEM. In: Proceedings 6th International Conference on Gas Hydrates, Vancouver, B.C, p. 12.
Suess, E., Torres, M.E., Bohrmann, G., Collier, R.W., Greinert, J., Linke, P., Rehder, G., Trehu, A., Wallmann, K., Winckler, G., Zuleger, E., 1999. Gas hydrate destabilization; enhanced dewatering, benthic material turnover and large methane plumes at the Cascadia convergent margin. Earth Planet. Sci. Lett. 170 (1–2), 1–15.
Tanaka, M., Tanaka, H., Kamei, T., Hayashi, S., 2003. Effects of diatom microfossil contents on engineering properties of soils. In: Proceedings Thirteenth International Offshore and Polar Engineering Conference, Honolulu, Hawaii, May 25–30, 2003.
Taylor, E., 1991. Physical Properties and Consolidation of the Calcareous Sediments of Broken and Ninetyeast Ridges.
Terzaghi, K., Peck, R., 1967. Soil Mechanics in Engineering Practice. John Wiley & Sons, New York, p. 729.
Tobin, H.J., Moore, J.C., Moore, G.F., 1995. Laboratory measurement of velocity vs. effective stress in thrust faults of the Oregon accretionary prism: implications for fault zone overpressure. In: Carson, B., Westbrook, G.K., Musgrave, R.J., Suess, E. (Eds.), Proceedings of the Ocean Drilling Program, Scientific Results, vol. 146(pt. 1), pp. 349–358.
Torres, M.E., Collett, T.S., Rose, K.K., Sample, J.C., Agena, W.F., Rosenbaum, E.J., 2011. Pore fluid geochemistry from the mount Elbert Gas hydrate stratigraphic test well, Alaska North slope. Mar. Pet. Geol. 28 (2), 332–342.
Torres, M.E., McManus, J., de Angelis, M.A., Tryon, M.D., Trehu, A.M., Brown, K.M., Hammond, D., Anonymous, 2002. Benthic fluxes from sediments hosting methane hydrate deposits at Hydrate Ridge, Cascadia: abstracts with Programs. Geol. Soc. Am. 34 (5), 42.
Torres, M.E., Trehu, A.M., Cespedes, N., Kastner, M., Wortmann, U.G., Kim, J.H., Long, P., Malinverno, A., Pohlman, J.W., Riedel, M., Collett, T., 2008. Methane hydrate formation in turbidite sediments of northern Cascadia, IODP Expedition 311. Earth Planet. Sci. Lett. 271 (1–4), 170–180.
Torres, M.E., Wallmann, K., Trehu, A.M., Bohrmann, G., Borowski, W.S., Tomaru, H., 2004. Gas hydrate growth, methane transport, and chloride enrichment at the southern summit of Hydrate Ridge, Cascadia margin off Oregon. Earth Planet. Sci. Lett. 226 (1–2), 225–241.
Trehu, A.M., Long, P.E., Torres, M.E., Bohrmann, G., Rack, F.R., Collett, T.S., Goldberg, D.S., Milkov, A.V., Riedel, M., Schultheiss, P., Bangs, N.L., Barr, S.R., Borowski, W.S., Claypool, G.E., Delwiche, M.E., Dickens, G.R., Gracia, E., Guerin, G., Holland, M., Johnson, J.E., Lee, Y.-J., Liu, C.-S., Su, X., Teichert, B., Tomaru, H., Vanneste, M., Watanabe, M., Weinberger, J.L., 2004. Three-dimensional distribution of gas hydrate beneath southern hydrate ridge: constraints from ODP Leg 204. Earth Planet. Sci. Lett. 222, 845–862.
Uchida, T., Takashi, T., 2004. Petrophysical properties of natural gas hydrates-bearing sands and their sedimentology in the Nankai Trough. Resour. Geol. 54 (1), 79–87.
von Herzen, R.P., Maxwell, A.E., 1959. The measurement of Thermal conductivity of deep sea sediments by needle probe method. J. Geophys. Res. 64 (10), 1557–1563.
Waite, W.F., Kneafsey, T.J., Winters, W.J., Mason, D.H., 2008. Physical property changes in hydrate-bearing sediment due to depressurization and subsequent repressurization. J. Geophys. Res.-Solid Earth 113 (B7).
Wentworth, C.K., 1929. Method of computing mechanical composition of sediments. Geol. Soc. Am. Bull. 40, 771–790.
Winters, W., Dugan, B., Collett, T., 2008a. Physical properties of sediments from Keathley Canyon and Atwater Valley, JIP Gulf of Mexico gas hydrate drilling program. Mar. Pet. Geol. 25 (9), 896–905.
Winters, W., Walker, M., Hunter, R., Collett, T., Boswell, R., Rose, K., Waite, W., Torres, M., Patil, S., Dandekar, A., 2011. Physical properties of sediment from the mount Elbert Gas hydrate stratigraphic test well, Alaska North slope. Mar. Pet. Geol. 28 (2), 361–380.
Winters, W.J., 2011. Physical and geotechnical properties of gas-hydrate-bearing sediment from offshore India and the northern Cascadia margin compared to other hydrate reservoirs. In: Proceedings 7th International Conference on Gas Hydrates, Edinburgh, Scotland, July 17–21, 2011.
Winters, W.J., Dallimore, S.R., Collett, T.S., Jenner, K.A., Katsube, J.T., Cranston, R.E., Wright, J.F., Nixon, F.M., Uchida, T., 2000a. Relation between gas hydrate and physical properties at the Mallik 2L-38 research well in the Mackenzie Delta. Ann. N. Y. Acad. Sci. 912, 94–100.
Winters, W.J., Dallimore, S.R., Collett, T.S., Katsube, T.J., Jenner, K.A., Cranston, R.E., Wright, J.F., Nixon, F.M., Uchida, T., 1999a. Physical properties of sediments from the JAPEX/JNOC/GSC Mallik 2L-38 gas hydrate research well. Bull. – Geol. Surv. Can. Rep. 544, 95–100.
Winters, W.J., Dallimore, S.R., Collett, T.S., Medioli, B.E., Matsumoto, R., Katsube, J.T., Brennan-Alpert, P., 2005. Relationships of sediment physical properties from the JAPEX/JNOC/GSC et al. Mallik 5L-38 gas hydrate production research well. In: Dallimore, S.R., Collett, T.S. (Eds.), Scientific Results from the Mallik 2002 Gas Hydrate Production Research Well Program, Mackenzie Delta, Northwest Territories, 585. Geological Survey of Canada, Bulletin, Canada, Ottawa, p. 9.
Winters, W.J., Lorenson, T.D., Paul, C.K., 2007a. Initial Report of the IMAGES VIII/PAGE 127 Gas Hydrate and Paleoclimate Cruise on the RV Marion Dufresne in the Gulf of Mexico, 2–18 July 2002. U.S. Geological Survey Open-File Report 2004–1358.
Winters, W.J., Lorenson, T.D., Paull, C.K., Balut, Y., 2007b. Coring and Gas hydrate-related operations during the images VIII/PAGE 127 Gas hydrate and Paleoclimate cruise on the RV Marion dufresne in the gulf of Mexico, 2–18 July 2002. In: Winters, W.J., Lorenson, T.D., Paull, C.K. (Eds.), Initial Report of the IMAGES VIII/PAGE 127 Gas Hydrate and Paleoclimate Cruise on the RV Marion Dufresne in the Gulf of Mexico, 2–18 July 2002. Geological Survey, Reston, VA, U.S, p. 19. U.S. Geological Survey Open-File Report 2004-1358.
Winters, W.J., Novosel, I., Boldina, O., Waite, W.F., Kelsey, S.A., Hallett, B.W., 2007c. Physical Properties of Sediment Obtained During the Coring and Gas Hydrate Related Operations During the IMAGES VIII/PAGE 127 Gas Hydrate and Paleoclimate Cruise on the RV Marion Dufresne in the Gulf of Mexico, 2-18 July 2002. U.S. Geological Survey Open-File Report 2004-1358.
Winters, W.J., Paull, C.K., Matsumoto, R., Wallace, P.J., Black, N.R., Borowski, W.S., Collett, T.S., Damuth, J.E., Dickens, G.R., Egeberg, P.K., Goodman, K., Hesse, R.F., Hiroki, Y., Holbrook, W.S., Hoskins, H., Ladd, J., Lodolo, E., Lorenson, T.D., Musgrave, R.J., Naehr, T.H., Okada, H., Pierre, C., Ruppel, C.D., Satoh, M., Thiery, R., Watanabe, Y., Wehner, H., Winters, W.J., Wood, W.T., 2000b. Stress history and geotechnical properties of sediment from the Cape Fear Diapir, Blake Ridge Diapir, and Blake Ridge. In: Paull, C.K., Matsumoto, R., Wallace, P.J., Dillon, W.P. (Eds.), Proceedings of the Ocean Drilling Program, Scientific Results, vol. 164, pp. 421–429.
Winters, W.J., Pecher, I.A., Booth, J.S., Mason, D.H., Relle, M.K., Dillon, W.P., 1999b. Properties of samples containing natural gas hydrate from the JAPEX/JNOC/GSC Mallik 2L-38 gas hydrate research well, determined using gas hydrate and sediment test Laboratory instrument (GHASTLI). Bull. – Geol. Surv. Can. Rep. 544, 241–250.
Winters, W.J., Pecher, I.A., Waite, W.F., Mason, D.H., 2004. Physical properties and rock physics models of sediment containing natural and laboratory-formed methane gas hydrate. Am. Mineral. 89 (8–9), 1221–1227.
Winters, W.J., Waite, W.F., Mason, D.H., Gilbert, L.Y., 2006. Physical properties of repressurized sediment from Hydrate Ridge. In: Trehu, A.M., Bohrmann, G., Torres, M.E., Colwell, F.S. (Eds.), Proceedings ODP, Scientific Results, vol. 204, pp. 1–19.
Winters, W.J., Waite, W.F., Mason, D.H., Gilbert, L.Y., Pecher, I.A., 2007d. Methane gas hydrate effect on sediment acoustic and strength properties. J. Pet. Sci. Eng. 56 (1–3), 127–135.
Winters, W.J., Waite, W.F., Mason, D.H., Kumar, P., 2008b. Physical properties of repressurized samples recovered during the 2006 National Hydrate Program Expedition offshore India. In: Proceedings 6th International Conference on Gas Hydrates, Physical Properties of Repressurized Sample, July 6–10, 2008.
Xu, W., Ruppel, C., 1999. Predicting the occurrence, distribution, and evolution of methane gashydrate in porous marine sediments. J. Geophys. Res. 104, 5081.
Yun, T.S., Fratta, D., Santamarina, J.C., 2010. Hydrate-bearing sediments from the Krishna–Godavari Basin: physical characterization, pressure core testing, and scaled production monitoring. Energy Fuels 24 (11), 5972–5983.